

LOW-LIGHT-LEVEL NONLINEAR OPTICS WITH
RUBIDIUM ATOMS IN HOLLOW-CORE
PHOTONIC BAND-GAP FIBERS

A Dissertation

Presented to the Faculty of the Graduate School
of Cornell University

in Partial Fulfillment of the Requirements for the Degree of
Doctor of Philosophy

by

Amar Ramdas Bhagwat

February 2010

© 2010 Amar Ramdas Bhagwat

ALL RIGHTS RESERVED

LOW-LIGHT-LEVEL NONLINEAR OPTICS WITH RUBIDIUM ATOMS IN
HOLLOW-CORE PHOTONIC BAND-GAP FIBERS

Amar Ramdas Bhagwat, Ph.D.

Cornell University 2010

Low-light-level optical nonlinearities are of significant interest for performing operations such as single-photon switching and quantum non-demolition measurements on single-photons. To evoke strong nonlinearities from single-photons, one can enhance the matter-photon interaction using strongly nonlinear materials such as alkali vapors in combination with an appropriate geometry such as a waveguide, which provides a long interaction length while maintaining a small light mode area. We demonstrate for the first time that such a system can be experimentally realized by loading rubidium vapor inside a hollow-core photonic band-gap fiber. Using the technique of light-induced atomic desorption in this geometry, we have generated optical depths greater than 1000. As a proof of principle, we demonstrate electromagnetically induced transparency (EIT) with control powers 1000 times lower than those used for hot vapor cells in a focused beam geometry. Working with such a high aspect ratio geometry requires us to identify and measure the various sources of decoherence via spectroscopy of desorbed atoms in the fiber. Using such techniques, we also estimate the temperature of the desorbing atoms inside the fiber. The desorption mechanism is studied, and we show that pulsed desorption beams of the right amplitude and duration can be used for generating precisely controlled optical depths. Finally, we investigate the use of various buffer gas techniques for increasing the effective transverse path of the atoms as they move

across the fiber in order to reduce their ground state decoherence and map this effect as a function of buffer gas pressure.

BIOGRAPHICAL SKETCH

Amar Bhagwat was born in *Aamchi Mumbai* ("Our Mumbai" in marathi), India on 27 November 1981. He attended school in Mumbai where he discovered that the only things he was good at were math and science. After passing the Maharashtra State high school exams with distinction and merit, he joined the Indian Institute of Technology, Bombay in the fall of 1999. As an undergraduate in Mechanical Engineering, he heard the call of the Physics Sirens and promptly switched fields to pursue a bachelor's degree in physics. Amar graduated from IIT, Bombay in the summer of 2003 with a B.Tech. in Engineering Physics and joined Cornell University as a graduate student in the School of Applied and Engineering Physics in the fall of 2003. At Cornell, he performed research in the laboratory of Prof. Alexander L. Gaeta for which he earned the doctorate degree in the summer of 2009.

*To my parents,
who always encouraged my “scientific” experiments*

ACKNOWLEDGEMENTS

Graduate school has been an extremely fulfilling experience for me in terms of science. But more importantly, it is the people I met, the friends I made, and the mentors I worked with who made the experience a thousand times more enjoyable. I would like to thank my advisor Prof. Alexander L. Gaeta for being an outstanding source of inspiration and a great resource for advice on all fronts. Throughout my graduate career, Alex has lent me his steadfast support and encouragement when times got tough. I would also like to thank my committee members - Prof. Frank W. Wise and Prof. Michal Lipson for their advice and support.

Saikat Ghosh, with whom I worked on many an experiment, has played an important role not only as my friend and scientific mentor but also as my philosophical guide. Dimitre Ouzounov, famous for his razor sharp wit and warm friendship, taught me most of what I know about doing optics on an optical table. Aaron Slepko has been a wonderful friend and a fun post-doc to work with. Many thanks to my fellow "Rubids" - Vivek, Pablo and Kasturi for help in the lab and for numerous stimulating discussions. Bob "Sned" Snedeker and Nathan "Nate" Ellis, I couldn't have finished some machining jobs without your experience and knowledge - thank you.

Special thanks to my brother Amit and his wife Priya, for showing me a life outside the lab and taking care of me during their stay at Cornell. Caroline, you are a very special friend - thanks for all our exciting adventures together. Faisal Ahmad, Jahan Dawlaty and Sharvari Nadkarni have been wonderful comrades who "hanged out" with me on many a late night for tea and "deep" discussions. Many thanks to *tovarish* Kirill Bolotin who picked me up from the bus terminal on my first day in Ithaca and called me "family". To a fellow Black Adder fan,

Imad Agha with whom I discussed circuits, optics, bus rides and much more, thanks a bunch. Ferdinand Kuemmeth, master player of the harp, many thanks for all the climbing, badminton and sailing. Thanks to Sourish and Akshay for being awesome housemates and for the communal laundry experience. To all my labmates - Mark, Yoshi, Jay, Dan, Chris, Luat, Taylor, Ami, Reza and Onur, thanks for making the lab a wonderful place to work in. My fellow co-op housemates at Gamma Alpha Science Co-op, who provided a lively, homely environment full of good food and stimulating discussions and helped me stay sane - you have my deep gratitude. Ithaca, you put me in the midst of nature and made me feel at home - thank you for your hospitality.

Most importantly, I would like to thank my parents and my grandparents, for everything that they have done for me. None of this would be possible without their efforts and support.

TABLE OF CONTENTS

Biographical Sketch	iii
Dedication	iv
Acknowledgements	v
Table of Contents	vii
List of Figures	ix
1 Introduction	1
1.1 Nonlinear optics with low light powers	1
1.2 Hollow-core photonic band-gap fibers (HC-PBGFs)	4
1.3 Thesis Layout	6
2 Light-matter interactions: Resonant nonlinearities	8
2.1 Two-level atom: Density matrix approach	10
2.2 3-level systems: Interference in dressed states	14
2.3 Nonlinear optics at single-photon levels: Single photon switches and non-demolition measurements on single photons	18
3 Working with rubidium vapor: Challenges and Techniques	22
3.1 Rubidium	23
3.2 The UHV system assembly	24
3.3 Experimental section	28
3.4 Limitations of the setup and improvements	35
4 Generation of large alkali vapor densities inside bare hollow-core photonic band-gap fibers	37
4.1 The single-cell experimental setup	38
4.2 Temperature measurement of desorbed Rb atoms	40
4.3 Conclusion	47
5 On-demand all-optical generation of controlled Rb-vapor densities in photonic bandgap fibers	49
5.1 Introduction	49
5.2 Experimental Setup	50
5.3 Effect of desorption on Fiber Transmission	51
5.4 Temporal dynamics of LIAD	54
5.5 Intensity dependence of desorption	61
5.6 Summary	64
6 Buffer-gas effects of neon in HC-PBGFs	65
6.1 Experimental layout	68
6.2 Effect of buffer-gas on desorption	70
6.3 Effect of buffer gas on the transit time of atoms	72
6.4 Summary	76

7 Future Directions	78
A Chemistry protocol for coating the fiber cores	80
Bibliography	81

LIST OF FIGURES

1.1	A comparison between the interaction lengths for a free-space focused beam geometry versus that for a waveguide	3
1.2	(a) A Bragg-like band-gap structure [11] where a regular arrangement of refractive index ($n_1 > n_2$) strongly scatters the light such that it constructively interferes in the central core and destructively interferes everywhere else. Since transverse modes of propagation are forbidden, this leads to transverse confinement in the fiber and longitudinal guidance along its length. (b) Scanning electron micrograph of the actual fiber used for our experiments – AIR-6-800 from Crystal Fiber. The central core transmits the light, while the vertices of the hexagonal capillaries scatter light such that it remains confined to the core.	5
2.1	A 2-level atomic system with the ground state $ g\rangle$ and excited state $ e\rangle$ and an incident beam at frequency ω_p , detuned from the actual transition by a frequency detuning of δ	11
2.2	EIT performed in a Λ -scheme. $ 1\rangle$ and $ 2\rangle$ are the ground states of an atom and $ 3\rangle$ is the excited state. A weak probe beam is tuned to the $ 1\rangle \rightarrow 3\rangle$ transition with a detuning δ_p . When a strong control beam is coupled to the $ 2\rangle \rightarrow 3\rangle$ transition, the probe experiences no absorption as long as the detuning δ_c of the control beam is equal to the probe detuning δ_p . This is called the two-photon resonance condition of EIT.	14
2.3	The left panel shows the change as a function of probe detuning in the imaginary $\chi^{(1)}$ (proportional to absorption) from dotted line for a 2-level system to the solid line for a 3-level system dressed by a strong control beam. The corresponding change in real $\chi^{(1)}$ (a measure of refractive index) is shown in the middle plot. The plot on the right shows the enhanced nonlinear $\chi^{(3)}$ on resonance for an EIT system. The x-axis is scaled to the atomic natural linewidth [20].	16
2.4	A 4-level switching scheme where the transmission of a weak probe beam tuned on $ 1\rangle \rightarrow 3\rangle$ transition is switched on and off due to the presence or absence of a very weak, ideally a single-photon signal tuned on $ 2\rangle \rightarrow 4\rangle$ resonance.	19
2.5	A 4-level cross-phase modulation scheme where the phase induced on a weak probe beam tuned on $ 1\rangle \rightarrow 3\rangle$ transition is determined by the presence or absence of a very weak, ideally a single-photon signal tuned near the $ 2\rangle \rightarrow 4\rangle$ resonance. This conditional phase imparted on the probe beam finds various applications in quantum phase gates and quantum non-demolition measurements of single-photons.	20

3.1	Energy level diagrams for the ground and excited states of ^{87}Rb and ^{85}Rb for the D_1 and D_2 transitions. The Rb nuclei have a nuclear magnetic spin denoted by I , and hyperfine coupling with the nuclear spin causes the ground and excited state to split into various hyperfine levels [35] denoted by the new quantum number F , which is noted on the right side of each energy level. The hyperfine splitting is noted for all levels except the $5P_{3/2}$ level for clarity, but can be found in the compilation by Steck [36]. Also the natural abundance is noted at the bottom.	24
3.2	An exploded view of the vapor cell used for introducing Rb vapor into the hollow-core fiber (shown in red). The glass window enables light to be coupled into the fiber, while the middle flange provides connections to vacuum as well as the Rb source. A similar cell encloses the other end of the fiber.	25
3.3	(a) The methoxy group of n-octadecyl dimethyl methoxysilane reacts with the dangling ^-OH bond on silica surfaces forming a self-assembled monolayer of the organosilane entities while a methanol molecule is released as a byproduct. (b) The band-gap obtained from fiber transmission measurements is essentially preserved on coating as shown by the data in red as opposed to the original band-gap as shown by the data in black.	29
3.4	The experimental setup used to observe desorption. A 795 nm probe laser tuned to the D_1 line of ^{87}Rb is coupled through the fiber and detected using a PMT. A desorption laser tuned to 770 nm (far from Rb resonances) is coupled counter-propagating to the probe beam.	30
3.5	(a) Calculated number of atoms in the fiber core with the inset showing the energy levels being probed. (b) Normalized transmission showing the Doppler absorption features and the corresponding theoretical fits in solid lines.	32
3.6	(a) Transmission spectra of the probe field in presence of a 361-nW control field. The arrow shows the transparency window due to electromagnetically-induced transparency (EIT) together with the corresponding theoretical fit. The peak to the left of the arrow corresponding to detuned $5S_{1/2}, F = 2 \rightarrow 5P_{3/2}, F' = 2$ transition is not taken into account in the fit. The inset shows transparency larger than 90% for a probe scanned over $5S_{1/2}, F = 1 \rightarrow 5P_{1/2}, F' = 1$ with a 2.65- μW control field tuned to $5S_{1/2}, F = 1 \rightarrow 5P_{3/2}, F' = 1$ transition. (b) Experimental (red) and theoretical (black) variation of the EIT linewidth as a function of the control intensity. The inset shows the energy-level scheme for this system.	34

4.1	Two 4.5-cm-long hollow-core photonic bandgap fibers – one coated and the other uncoated are mounted inside a steel chamber with glass windows connected to an ultrahigh vacuum system. A 795-nm probe and 805-nm desorption beam are coupled into the fiber in counter-propagating geometry with 10× microscope objectives, and the coupling is monitored using a CCD camera. The probe beam can alternately be passed through the cell and detected by a photodiode to monitor the ambient cell Rb density. The coupled probe light is detected with photomultiplier tube (PMT). L: lens; PD: photodiode.	39
4.2	Absorption profiles of $F = 2 \rightarrow F' = 2, 3$ transitions in the D_1 line of ^{85}Rb . (a) The absorption profile of the ambient Rb vapor used to load the hollow-core fiber, as seen by passing light adjacent to the fiber. The position and relative oscillator strengths of the two transitions are indicated by the black arrows. The data is fit (black line) with a Voigt profile that assumes a natural linewidth of 5.75 MHz and yields a FWHM Doppler width of 575 MHz. (b) The through-fiber absorption profile in the presence of weak Rb desorption. The solid line is a fit to a Voigt profile with a Lorentzian component linewidth of 20 MHz, corresponding to transit-time broadening, and to a Doppler-broadening Gaussian component with a FWHM of 670 MHz. The key feature of note is that the through-fiber absorption profile is considerably broader than that of the ambient Rb vapor.	41
4.3	Absorption profiles of lines in the D_1 transition of ^{87}Rb and ^{85}Rb . The frequency scale is zeroed on the lowest energy D_1 transition ($^{87}\text{Rb } F=2 \rightarrow F'=2$). (a) A relatively low optical depth of Rb. The black line is a fit to six Voigt lines that include the effects of transit-time broadening (see text). The position and relative absorption strength [52] are represented by the black arrows and their lengths, respectively. (b) A moderately high optical depth generated by LIAD with black line as a free fit to the data. (c) The absorption profile of a large density, with a conservatively estimated optical depth of ~ 1200 between the $F=3 \rightarrow F'=2,3$ resonances of ^{85}Rb	45
5.1	Two fibers: one coated and one uncoated (4.5 cm long) are placed inside a vacuum cell with glass windows on both sides. The desorption and probe lasers are coupled counter-propagating through a given fiber. A CCD camera is used to ascertain that the lasers are coupled to a single mode in the fiber core. A photodiode (PD) monitors the ambient Rb vapor density in the cell. PMT: photomultiplier tube, L: lens, PBS: polarizing beamsplitter, AOM: acousto-optic modulator	50

5.2	The transmission of the desorption beam shows a positive feedback behavior where as the coupling of the desorption beam increases more atoms get desorbed and the coupling improves further. The fiber end is imaged at various times as shown: (a) At the beginning, most of the light is scattered out and leaks into the cladding layer. (b) Coupling improves over time as more of the light is retained in the core. The image is taken with a neutral density filter of 2. (c) A fully desorbed fiber regains its single-mode coupling. The image taken is with an additional neutral density filter of 2.	52
5.3	Change in spectral transmission of a broadband probe beam due to the desorption process for a coated photonic band-gap fiber over its entire band-gap. The data represented by open circles are for a 806-nm desorption beam while those shown by the solid circles represent data for 770-nm desorption beam. The solid line shows the published bandgap for a 2-m-long fiber and illustrates the band-edges [58]. Both sets of data show a larger increase in transmission at the higher wavelength band-edge. The data for an uncoated fiber follow similar trends (not shown).	53
5.4	Desorption signature at two different timescales. The shaded area denotes the time for which desorption pulse is on, while the dashed line represents transmission in the absence of desorption. Data in red circles indicate transmission change in a coated fiber while the data in uncoated fiber are indicated by the black curve. The data have been corrected for fiber coupling changes due to desorption and only indicate the effect of Rb vapor absorption. Relatively low desorption powers (10-15 mW incident) are used to generate optical depths suitable for displaying time-dynamics with sufficient dynamic range.	56
5.5	The recovery of the desorption capacity of an uncoated fiber is studied. A 1-ms desorption pulse generates almost complete absorption of probe on the first exposure. After repeated exposure of the fiber to many 1-ms desorption pulses, the probe absorption at the beginning of the pulse shows depletion and is maximally depleted at elapsed time = 0 s. The probe absorption is then recorded during exposure to identical 1-ms desorption pulses at subsequent time intervals, and we observe that the absorption slowly recovers to match its initial desorption capacity before depletion.	58

5.6	The fiber is initially exposed to a 2-s desorption pulse and its desorption capacity is then probed with 1-ms desorption pulses at various time intervals. We observe the absorption in the later part of the pulse to get depleted, while the initial part remains unchanged. The slower desorption recovers over the course of time as shown.	59
5.7	The desorption sequence (a) Fiber core with weakly attached atoms and nanoclusters, (b) desorption beam is turned on, (c) weakly attached atoms desorb, (d) nanoclusters evaporate, (e) atoms form a uniform layer, (f) atoms re-arrange over a period of time into nanoclusters.	60
5.8	Optical depth generated as a function of incident desorption beam power in a coated fiber. (a) 50- μ s pulses tuned on resonance are used to measure the absorption generated. The second, slower desorption mechanism does not contribute to this vapor generation. (b) Maximum steady OD generated by few-s long desorption pulses created by the second desorption mechanism.	62
5.9	(a) Generation of controlled OD using 50- μ s, 10-mW desorption pulses in a coated fiber. We see that the OD generated is uniform during the pulse and from pulse-to-pulse. The large peak in OD at the beginning likely corresponds to Rb atoms that undergo fast desorption but do not regenerate within 500 μ s. (b) EIT in Λ -scheme (shown by the arrow) demonstrated in the residual vapor generated in a coated fiber after a strong desorption pulse. The oscilloscope is triggered after the desorption beam is completely switched off. A very low control beam power (80 nW, tuned to $F=2 \rightarrow F'=2$ transition) is used and the EIT peak shows no measurable light shift.	63
6.1	Relaxation times that can be achieved as a function of buffer gas pressure for a Rb vapor-Ne gas system. The neon vapor pressure is calculated at 50 °C which is the typical temperature at which the Rb cells are operated. The pressure is normalized to atmospheric pressure P_0 . For theory see Franzen [63].	67
6.2	The two cells can be individually separated from the vacuum (valves not shown) so that the buffer-gas line can be flushed a number of times before the gas is introduced into the cell containing Rb vapor. Convectron pressure gauges on the cells monitor the pressure of buffer gas in the cells and are insensitive to Rb vapor. A Fabry-Perot etalon separates the probe and control beams before the PMT.	69

6.3	Generated optical depth as a function of buffer gas pressure. The desorption power was chosen such that the vapor produced for all pressures lies well within the dynamic range of the graph. The probe scans over the ^{87}Rb D_1 line ($F=1 \rightarrow F'=1,2$) transition. γ denotes the linewidth of the excited state due to buffer gas collisions, which is extracted from a theoretical fit to the absorption lines.	71
6.4	(a) A strong pumping beam pumps atoms into the $F=1$ ground state. Once the pump is turned off, a weak probe monitors the absorption as a function of time, which is a measure of rate of transfer of atoms from $F=1$ to $F=2$ ground state. (b) A Λ -scheme EIT sets up coherence between the two ground states wherein the ground-state decoherence and power broadening determine the EIT linewidth.	72
6.5	A 70-nW EIT feature on the $F = 1 \rightarrow F' = 1$ transition. The corresponding saturated absorption signal (SAS) obtained in a vapor cell is shown in the lower graph and used as the frequency reference. The EIT feature and the center of the Doppler line are offset from the SAS due to control field detuning and AC Stark shift from the desorption beam, respectively.	74
6.6	The EIT linewidth FWHM plotted as a function of control beam power. The data in red squares represent the linewidths in the absence of any buffer gas while those in black squares represent the linewidths at 50 torr of Ne buffer gas. The solid lines of the corresponding colors represent the fits to an expression of the form $A + B\sqrt{P_{control}}$ where B is proportional to $\sqrt{\gamma_{bc}/\gamma}$	76

CHAPTER 1

INTRODUCTION

Many quantum communications protocols used for secure communications are based on single photons [1], which are robust carriers of quantum information. In addition to key elements such as storage and buffering of information, this communication infrastructure requires elements such as single-photon activated switches. Additionally, the necessity to register the arrival of a single photon without destroying it, in order to trigger additional operations requires the ability to perform quantum non-demolition measurements on single photons.

Such operations require very weak beams of light (ideally single photons) to imprint their properties on possibly much stronger light beams. Any interaction between light beams which induces changes in the phase and amplitude of other light beams can be brought about via nonlinear optical interactions. Simply speaking, the optical properties of a medium can be influenced by the presence of one light beam, which can then be sensed by another light beam.

1.1 Nonlinear optics with low light powers

The nonlinear response of the medium is proportional to the nonlinearity of the medium and the intensity of light used. In order to achieve strong nonlinear optical interactions with very low light powers, the strength of interaction of the medium with light needs to be maximized. A measure of how strongly a medium interacts with light is the optical depth κ , defined as

$$\kappa = n\sigma L, \quad (1.1)$$

where n is the number density of scatterers in the medium, σ is the absorption cross-section of those scatterers, and L is the effective length of interaction in the medium. Since intensity of light $I = P/A_{eff}$, where P is the light power and A_{eff} is the effective area of the light mode, one can easily see that the smallest mode area achievable will give the highest intensity. We observe that by choosing a suitable medium and proper geometry, one may be able to achieve strong nonlinear interactions with low light powers. Alkali atoms such as Li, Na, K, Rb and Cs have some of the highest possible σ values. Additionally, the requirement of a large L/A_{eff} ratio suggests that a waveguide geometry would provide us with the highest geometrical enhancement possible. Additionally for free atoms, the scattering cross-section A_{sc} (i.e. the total rate at which energy is removed from the beam in all directions) is given by [2]

$$A_{sc} = \frac{3\lambda^2}{2\pi}, \quad (1.2)$$

where λ is the wavelength on resonance. The atom-photon interaction will be highest when the mode area A_{eff} approaches A_{sc} .

Figure 1.1 shows a comparison between a waveguide and a free space geometry with focused beams. One can see that for a free-space focused geometry, the interaction length is limited by the diffraction length of the beam, whereas a low-loss waveguide can essentially maintain the intensity at the focal plane throughout its entire length, thus increasing the effective interaction length manifold. For a Gaussian beam, the diffraction length L_{diff} is given by twice

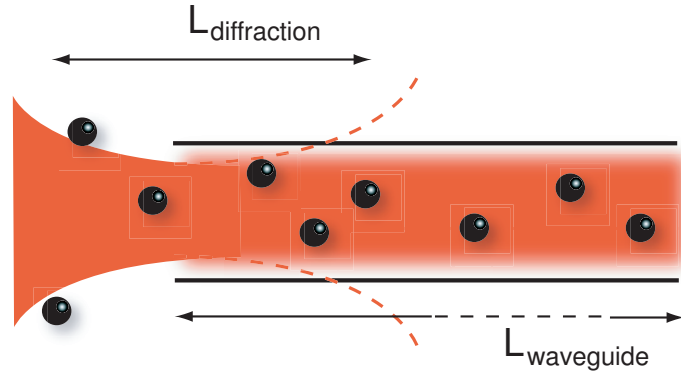


Figure 1.1: A comparison between the interaction lengths for a free-space focused beam geometry versus that for a waveguide

the Rayleigh range,

$$L_{diff} = \frac{2\pi w_0^2}{\lambda}, \quad (1.3)$$

where w_0 is the beam waist at the focus. For a reasonable waveguide diameter of $10 \mu\text{m}$, the L_{diff} is approximately $200 \mu\text{m}$ while waveguides can be many cm long.

This suggests that a hollow waveguide hosting a vapor of alkali atoms can provide us with such a geometry for performing nonlinear optics with very low light powers. But how can one make a system where the waveguide is hollow and can host alkali atom vapors as the interacting medium? This would require light guidance in a low-index region surrounded by a high-index cladding structure which operates on a principle other than total internal reflection. As described in the next section, hollow-core photonic band-gap fibers allow us to host alkali atoms inside the core and perform nonlinear optical interactions with them.

1.2 Hollow-core photonic band-gap fibers (HC-PBGFs)

Hollow-core photonic band-gap fibers [3, 4] are a recent addition to the fiber-optic toolbox, developed to exhibit unique dispersive and nonlinear optical properties. The concept of a photonic band-gap borrows its basic principles from condensed matter physics, where the transport of electrons with certain energies through an atomic lattice (a strongly scattering periodic potential) is forbidden depending on the electron momentum and the lattice spacing in that direction, thus giving rise to a “band-gap” in the energy-momentum distribution [5]. The seminal work of Anderson [6] and Mott [7] on the localization of electrons at defect sites in solids suggested that the same could be observed for electromagnetic waves in strongly scattering dielectric structures. The first suggestion for guiding light in a low index waveguide by surrounding it with Bragg structures was made by Yeh and Yariv [8]. Yablonovitch [9] and John [10] showed similar and complementary theoretical results describing prohibited photonic transmission at certain wavelengths and corresponding guidance due to localization at the defect site. Figure 1.2(a) shows the structure proposed and used for the first demonstration of single-mode photonic band-gap guidance in air [11].

The fibers are made using the stack and draw technique [4] in which hollow glass capillaries are stacked together, seven capillaries from the center are removed and the structure is fused and drawn into fibers. The drawn fibers maintain their original aspect ratio and display a band-gap determined by the spacing of the holes (called the pitch) and the refractive index contrast. Additionally, these fibers can be dispersion-engineered and show very low nonlinearities from the silica structure because most of the light (> 92%) is confined to

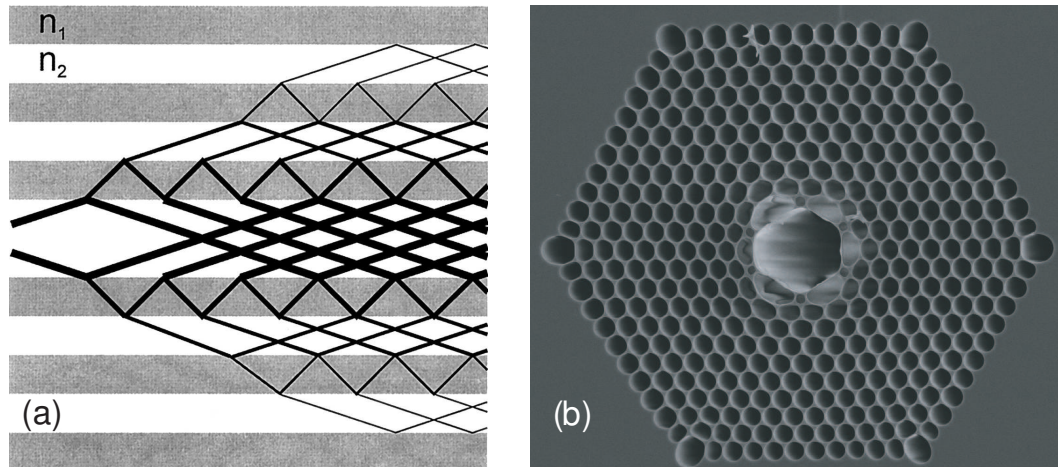


Figure 1.2: (a) A Bragg-like band-gap structure [11] where a regular arrangement of refractive index ($n_1 > n_2$) strongly scatters the light such that it constructively interferes in the central core and destructively interferes everywhere else. Since transverse modes of propagation are forbidden, this leads to transverse confinement in the fiber and longitudinal guidance along its length. (b) Scanning electron micrograph of the actual fiber used for our experiments – AIR-6-800 from Crystal Fiber. The central core transmits the light, while the vertices of the hexagonal capillaries scatter light such that it remains confined to the core.

the air-filled core [12].

The main advantage of HC-PBGFs is that they can host atoms, molecules, fluids and other nonlinear media for performing nonlinear optics [13]. The strong confinement of light in a small mode area can be used either to perform nonlinear optics at low light powers with strongly nonlinear media such as alkali vapors or to evoke a strong nonlinear response from gases such as acetylene or hydrogen, which exhibit much weaker nonlinearities, using moderate light powers of tens of mW.

1.3 Thesis Layout

In this thesis, we will discuss the progress made towards performing nonlinear optics with low light powers using hot alkali vapors inside HC-PBGFs. In chapter 2, we will discuss the physics of atom-photon interaction. We will see that in a simple 2-level atom, the atom-photon nonlinear interactions are the strongest on resonance, but that also gives rise to the problem of absorption. This can be solved with a three-level system using electromagnetically-induced transparency (EIT). We will discuss various applications that use EIT and extend it via a 4-level configuration to a single-photon switching scheme as well as quantum non-demolition schemes for sensing photons.

In the third chapter, we will discuss the various challenges faced and the experimental techniques that were used to inject atomic vapors inside HC-PBGFs whose cores were modified with organic coatings. We will discuss the initial results that led to the first observation of Rb vapor inside HC-PBGFs using the process of light-induced atomic desorption (LIAD) as well as the first demonstration of EIT with hot atomic vapors at control powers 1000 times lower than those used previously in vapor cells. We will also discuss the improvements needed to make the system more practicable.

The fourth chapter discusses the first demonstration of Rb vapor generation in HC-PBGFs without any coating modification as well as the generation of very high optical depths (> 1000). We will also discuss some spectroscopic effects which enable us to measure the temperature of the atoms and various broadening mechanisms due to the unique fiber geometry. In the fifth chapter we will investigate the inner workings of the desorption process and propose

a physical mechanism for the same. We also show that we can generate highly controlled Rb vapor densities on-demand.

The sixth chapter describes our efforts towards mitigating various decoherence mechanisms arising due to the confined fiber geometry by using a buffer gas such as neon. Finally, we conclude the thesis with a discussion on possible future experiments that can be performed using the knowledge we have gained so far.

CHAPTER 2

LIGHT-MATTER INTERACTIONS: RESONANT NONLINEARITIES

The interaction of light with matter starts with the electric field exerting a force on the electrons that are bound to the nuclei. The strength of the electric field is usually small and the resulting effect is that the electron cloud distribution is slightly perturbed by the incident electric field. Thus under the effect of the oscillating electric field, the electrons accelerate back and forth trying to follow the forced oscillations of the light field. From Maxwell equations, we know that accelerating charges radiate energy in the form of electromagnetic radiation [14], and this phenomenon is responsible for scattering and absorption observed in material media. The polarization $\vec{P}(t)$ induced in a sample is proportional to the field $\vec{E}(t) = \vec{E}e^{i\omega t} + c.c.$ such that

$$\vec{P}(t) = \tilde{\chi}\vec{E}(t), \quad (2.1)$$

where $\tilde{\chi}$ is defined as the electric susceptibility of the medium and is in general a tensor. The susceptibility tensor can itself be a function of the electric field $\vec{E}(t)$ as will be shown later and this field dependent part gives rise to nonlinearities in the medium. Following a Taylor expansion, the susceptibility can be written as

$$\tilde{\chi} = \tilde{\chi}^{(1)} + \tilde{\chi}^{(2)} : E + \tilde{\chi}^{(3)} : EE + \dots, \quad (2.2)$$

where the superscript on the $\tilde{\chi}$ refers to the order of correction to linear behaviour applicable under strong electric fields. The representation of suscepti-

bility in this manner makes it apparent that the stronger the electric fields, the more the higher-order effects contribute to the total response of the medium to external electric fields. The time dependent polarization of the medium which consists of terms oscillating at $\omega, 2\omega, 3\omega, \dots$, then dictates what frequencies the electron clouds of the sample will emit radiation at. The real part of the susceptibility contributes to the refractive index, whereas the imaginary part contributes to absorption in the media.

The interaction energy between a particle of charge q and electric field $\vec{E}(t)$ is given by $-\int q\vec{E}(t) \cdot d\vec{x}$, where x is the charge displacement. In the case of an electron bound to an atom, this can be rewritten such that $q\vec{d}x$ is an electric dipole $\vec{\mu}$ under the influence of an external field $\vec{E}(t)$. Thus, we can then extend this into the quantum mechanical regime and define an operator

$$\hat{V} = -\hat{\mu} \cdot \vec{E}(t), \quad (2.3)$$

where \hat{V} defines the energy of interaction between the electron and the external field and the operator $\hat{\mu} = q\hat{r}$ contains the distance operator \hat{r} and is defined as the dipole moment operator of the atom.

In order to treat the atom-field system mathematically, one may then define a new hamiltonian $\hat{H} = \hat{H}_0 + \hat{V}$, such that \hat{H}_0 is the unperturbed hamiltonian of the atom. In the case of non-resonant, weak excitation one may then proceed to solve the Schrödinger equation using a Rayleigh-Schrödinger perturbation theory in which the new quantum states of the atom are described by the old eigenstates of the free atom plus a correction that comes about due to the new interaction term. A rigorous treatment of this calculation can be found in

Boyd [15]. One may then proceed to calculate the ensemble average value of the microscopic observable $\hat{\mu}$ and then calculate the value of the macroscopic observable \vec{P} using $\vec{P} = N\vec{\mu}$ where N is the number of atoms. From this treatment, one finds the linear susceptibility for frequency ω_p is of the form of

$$\chi^1(\omega_p) = \frac{N}{\hbar} \sum_{eg} (\rho_{ee}^{(0)} - \rho_{gg}^{(0)}) \frac{\mu_{eg}\mu_{ge}}{(\omega_{eg} - \omega_p) - i\gamma_{eg}}, \quad (2.4)$$

where $\rho_{ee(gg)}$ is the equilibrium population of excited (ground) state respectively, μ_{ge} is the dipole moment for the $e \rightarrow g$ transition, ω_p is the incident laser frequency and $\hbar\omega_{eg}$ is the energy difference between ground and excited states. This equation drives home the point that in the case of resonant excitation, not only does the real part vanish, but also the treatment does not account for changes to population distributions due to the incident laser field. In reality, such a redistribution of population gives rise to saturation effects in absorption and gives rise to nonlinearities. It is clear that to treat very strong, resonant excitation, one needs an exact treatment instead of a perturbative approach, which we shall describe below.

2.1 Two-level atom: Density matrix approach

A two-level system is the most basic reduction of atom-photon interactions, but more complex schemes can be built and studied using the same basic principles that are used for the two-level treatment. One of the basic postulates of quantum mechanics states that the quantum state of any system can be represented by a state vector $|\psi\rangle$, which if known can be used to make predictions about the interaction of the system with external fields and its evolution with time. But

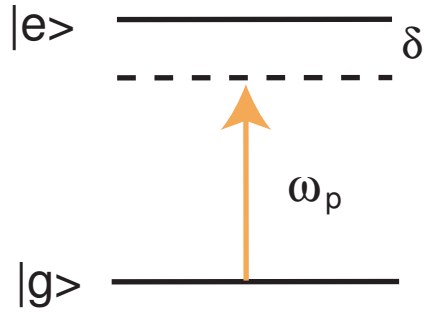


Figure 2.1: A 2-level atomic system with the ground state $|g\rangle$ and excited state $|e\rangle$ and an incident beam at frequency ω_p , detuned from the actual transition by a frequency detuning of δ .

many times, one needs to treat a large ensemble of atoms for which the quantum state of each atom may not be known exactly. For such systems, a more statistical approach is necessary wherein the system is described by a general quantity called the density matrix $\hat{\rho}$ with the following evolution relation [16]

$$i\hbar \frac{d}{dt} \hat{\rho} = [\hat{H}, \hat{\rho}]. \quad (2.5)$$

The diagonal elements of the matrix $\hat{\rho}$ denote the population distributions corresponding to various energy-level states, while the off-diagonal elements denote coherences between states, which refers to how much the corresponding states evolve with a common phase. The higher the coherences, the higher the linear superposition between the states and the more quantum-mechanical the system. A purely classical system will then have zero off-diagonal elements. A two-level system is shown in Fig. 2.1 with two states $|g\rangle$ and $|e\rangle$ and incident light of frequency ω_p and detuning δ from the resonance. Using Eqn. 2.3 as the interaction energy, one can write a hamiltonian

$$\hat{H} = \begin{bmatrix} \hbar\delta & -\mu E(\omega_p) \\ -\mu E(\omega_p) & 0 \end{bmatrix}; \quad (2.6)$$

this hamiltonian is defined in terms of the original eigenstates of the atom as the basis vectors and the presence of the off-diagonal elements shows that the original eigenstates of the free atom, $|g\rangle$ and $|e\rangle$ are no longer the eigenstates of the atom-photon system and the new eigenstates are a coherent superposition of $|g\rangle$ and $|e\rangle$. Diagonalizing the hamiltonian, we find the new eigenstates have energies shifted from the original by

$$\Delta E_{e,g} = \frac{\hbar}{2}(-\delta \mp \sqrt{\delta^2 + \Omega^2}), \quad (2.7)$$

where Ω is called the Rabi frequency defined by $\mu E/\hbar$. This shift in the energy from the original states is called the AC Stark shift or the light shift. Light shifts will play a significant role in some of the later discussions in this chapter. The new eigenstates of the system can be written in terms of the old states as

$$\begin{aligned} |1\rangle &= \cos\theta |g\rangle - \sin\theta |e\rangle \\ |2\rangle &= \sin\theta |g\rangle + \cos\theta |e\rangle, \end{aligned} \quad (2.8)$$

where the mixing angle θ is defined by $\cos(2\theta) = \delta/\sqrt{\delta^2 + \Omega^2}$. Note that the larger the δ , the smaller is the mixing angle and the closer the new states are to the original states. For the on-resonance condition ($\delta = 0$), $\theta = \pi/4$ and there is perfect superposition of the two states such that the system spends equal time in the excited states and ground states, which also means that the population distributions change drastically from mostly being in the ground state to

being equally distributed between the ground and excited states, resulting in reduced absorption. This is the most basic nonlinear effect where absorption decreases as the intensity of the laser increases. Another interpretation of this result is to realize that there are 2 possible configurations with equal energies: an atom in ground state plus a photon or only an atom in the excited state. Any coupling between these two degenerate configurations (provided by the dipole interaction term) will set up linear superpositions of the two states and break the degeneracy to generate the new “dressed” states separated by the energy of coupling. The population is said to undergo “Rabi flopping” between ground and excited states at a rate given by $\Omega' = \sqrt{\delta^2 + \Omega^2}$. In the presence of relaxation mechanisms such as spontaneous emission, one can show that the mixing angle tends more towards the ground state because of the additional excited state decay rate denoted by Γ . When $\Omega' \gg \Gamma$, the populations are equally distributed again and the system shows saturation of absorption.

It turns out that once we solve for $\langle \hat{\mu} \rangle$, the susceptibility shows that the nonlinearities are highest on resonance, but there still exists the problem of scattering due to absorption. To achieve large nonlinearities, one needs to propagate light through a significant interaction length and propagating light through such optically dense media will eventually result in absorption losses. Also, the absorption comes about because of spontaneous scattering off the atoms which leaves the atoms with a random phase and hence any quantum phase information is lost.

These obstacles can be overcome by engineering the energy levels of atoms using external laser fields to achieve high nonlinearities while eliminating linear absorption as will be shown in the next section.

2.2 3-level systems: Interference in dressed states

Fano [17] realized that two closely spaced levels that can rapidly decay to the same continuum are systems where the same eventual state can be achieved via two different pathways. These two pathways can interfere constructively or destructively depending on the frequency of the incident light. Harris and Imamoglu [18] showed that a set of energy levels that are dressed by an external laser beam show very similar behavior to the the states considered by Fano. This phenomenon was called “Electromagnetically induced transparency (EIT)” by Harris and was first observed by Boller *et al.* in a strontium vapor [19].

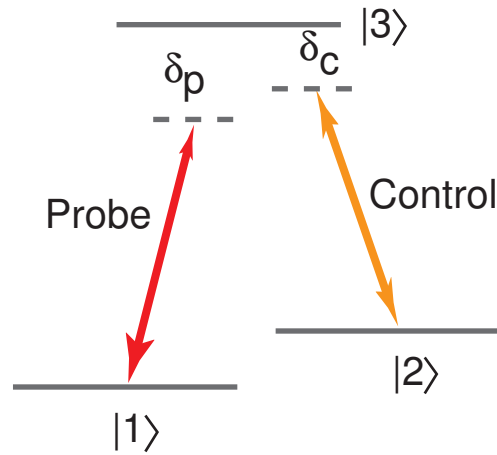


Figure 2.2: EIT performed in a Λ -scheme. $|1\rangle$ and $|2\rangle$ are the ground states of an atom and $|3\rangle$ is the excited state. A weak probe beam is tuned to the $|1\rangle \rightarrow |3\rangle$ transition with a detuning δ_p . When a strong control beam is coupled to the $|2\rangle \rightarrow |3\rangle$ transition, the probe experiences no absorption as long as the detuning δ_c of the control beam is equal to the probe detuning δ_p . This is called the two-photon resonance condition of EIT.

Figure 2.2 shows a typical 3-level scheme where EIT can be performed in the so-called Λ configuration. Initially a weak probe beam is tuned to the 1-3 transition with a detuning of δ_p . As the probe is scanned, it experiences the

typical Lorentzian absorption profile of the excited state when it passes through zero detuning. When a strong control beam tuned from the excited state to a third state $|2\rangle$ (not coupled to $|1\rangle$) via a dipole transition) with detuning δ_c is then turned on, the probe beam experiences a window of transmission in the absorption whenever the two detunings are equal or $\delta_p - \delta_c = 0$ and the detunings are within the linewidth of the transition. For a cloud of cold atoms this is the natural linewidth of the atoms, while for a hot atomic vapor, this is true over the entire Doppler distribution width. One may understand this effect by keeping in mind that absorption comes about because atoms in the excited state undergo spontaneous emission and scatter light in random directions. But if the two pathways used for reaching the excited state i.e. $1 \rightarrow 3$ and $1 \rightarrow 3 \rightarrow 2 \rightarrow 3$ interfere at $|3\rangle$ with just the right phase such that the probability of being found in $|3\rangle$ is zero, then the atom never scatters light and the probe never undergoes absorption. The hamiltonian of the system can be written as

$$\hat{H} = -\hbar \begin{bmatrix} \delta_p & 0 & \Omega_p^* \\ 0 & \delta_c & \Omega_c^* \\ \Omega_p & \Omega_c & 0 \end{bmatrix}, \quad (2.9)$$

where $\Omega_{p(c)}$ is the Rabi frequency for probe (control) beams as defined in the previous section. This hamiltonian can be diagonalized to extract its eigenvalues and new eigenstates. For the special case of two-photon resonance, we see that out of the three new eigenstates, one of the eigenstates $|a_0\rangle$ is a linear superposition of the two ground states [20] such that

$$|a_0\rangle = \cos \theta |1\rangle - \sin \theta |2\rangle, \quad (2.10)$$

where $\tan \theta = \Omega_p/\Omega_c$, and once the system enters this “dark” state, the atom never spends time in the excited state $|3\rangle$ and hence the probe never sees absorption. Figure 2.3 [20] shows the change in linear and nonlinear susceptibilities that a probe experiences when the system changes from a 2-level (dotted lines) to a dressed 3-level system (solid lines). We observe that the linear absorption ($\text{Im}[\chi^{(1)}]$) vanishes, the $\chi^{(3)}$ is actually enhanced on resonance, while the refractive index $n = \sqrt{1 + 4\pi \text{Re} \chi^{(1)}}$ undergoes a sharp change in slope.

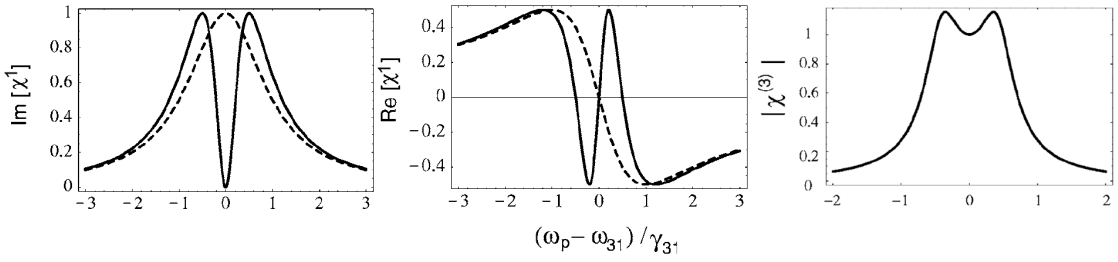


Figure 2.3: The left panel shows the change as a function of probe detuning in the imaginary $\chi^{(1)}$ (proportional to absorption) from dotted line for a 2-level system to the solid line for a 3-level system dressed by a strong control beam. The corresponding change in real $\chi^{(1)}$ (a measure of refractive index) is shown in the middle plot. The plot on the right shows the enhanced nonlinear $\chi^{(3)}$ on resonance for an EIT system. The x-axis is scaled to the atomic natural linewidth [20].

Using the enhanced $\chi^{(3)}$ which coincides with the eliminated absorption, Harris *et al.* [21] predicted highly enhanced four-wave mixing in this system. The group velocity in a medium is inversely proportional to the group index defined as $(n + \omega dn/d\omega)$. We observe that in an EIT window, the large positive slope $dn/d\omega$ gives rise to ultra-slow group velocities. Using a cloud of ultra-cold atoms Hau *et al.* slowed down light pulses to 17 m/s [22]. Slow light finds applications not only in retiming optical pulses, but also for enhancing nonlinear processes by increasing the effective path length of optical pulses through opti-

cally dense media, while EIT prevents absorption and subsequent scattering of the light pulses.

Also, it can be shown that the solution of light propagating through a dense EIT medium can be written down as a new quasi-particle composing of a linear superposition of the photon states and atom states called the dark-state polariton [23]

$$\hat{\Psi}(z, t) = \cos \theta \hat{E}(z, t) - \sin \theta \hat{s}(z, t), \quad (2.11)$$

$$\cot \theta = \frac{\Omega}{g \sqrt{N}}, \quad (2.12)$$

$$\hat{s} = |1\rangle\langle 2| e^{-i\omega_{12}t}, \quad (2.13)$$

where Ω defines the control beam Rabi frequency as usual, g is the strength of atom-field coupling, \hat{E} is the electric field operator and \hat{s} is a spin-wave operator as defined. We see that the incoming probe light pulse exists as a superposition of the field and ground-state spin states till the control beam is turned off and the quantum information in the probe is completely stored reversibly as the coherence of the ground states. This principle has been used to demonstrate stopped and stored light [24] and on-demand single-photon generation [25].

The slope $dn/d\omega$ depends on the linewidth of the EIT transition, which depends on the rate at which an atom makes incoherent transitions between the two ground states. This is because the quantum interference is maintained as long as the atom maintains the phase of the two interfering pathways. As soon as an atom makes a random transition between the ground states, the phases of the interfering pathways get randomised and the EIT is destroyed. Storage of pulses can be performed coherently only if the emitted light maintains phase

with the original beam, which implies that transitions between ground states cannot be allowed unless mediated coherently via the control beam which is possible only when the ground-state decoherence is very small. The two lower levels can be chosen such that no direct electric-dipole transition is allowed between the ground states if they have the same L quantum number, but different J quantum numbers. This does not prevent magnetic-dipole and electric-quadrupole transitions from occurring, which means decoherence increases due to stray magnetic fields and collisions with other atoms.

2.3 Nonlinear optics at single-photon levels: Single photon switches and non-demolition measurements on single photons

EIT can be used for enhancing nonlinearities significantly, but additionally, the basic Λ -scheme is also the basis for performing single-photon nonlinearities such as an all-optical switch triggered by a single photon, or sensing the presence of a single-photon using the cross-phase modulation induced on a strong beam by a single photon. All these techniques are based on a 4-level N -scheme which uses the highly sensitive quantum interference for detecting the nonlinear effects of single photons.

Figure 2.4 shows a 4-level switching scheme as proposed by Harris and Yamamoto [26] for switching off a weak probe beam on the presence of a very weak (ideally single photon) signal beam. This scheme works on the principle that a Λ -scheme EIT formed by the 1-2-3 system is a very narrow-band trans-

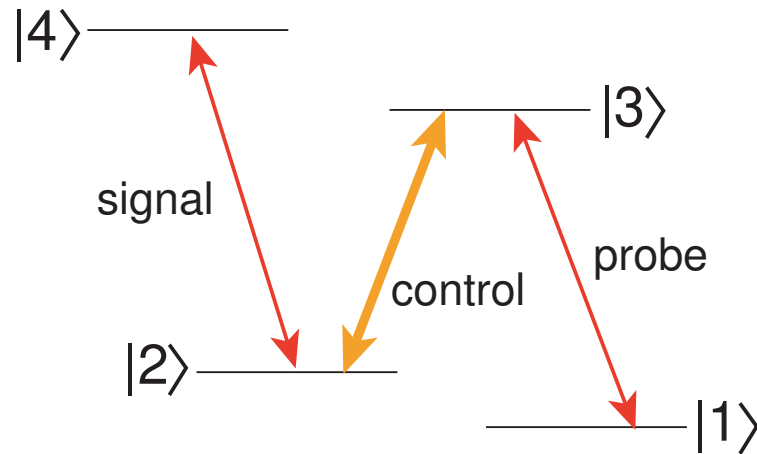


Figure 2.4: A 4-level switching scheme where the transmission of a weak probe beam tuned on $|1\rangle \rightarrow |3\rangle$ transition is switched on and off due to the presence or absence of a very weak, ideally a single-photon signal tuned on $|2\rangle \rightarrow |4\rangle$ resonance.

parency for the weak probe beam tuned to the 1-3 transition. The introduction of a weak signal beam on the 2-4 transition will induce a small light-shift on the $|2\rangle$ and $|4\rangle$ levels. If the induced light shift is significant such that the $|2\rangle$ moves out of 2-photon EIT resonance for the probe by more than the EIT linewidth, then the EIT condition will no longer be satisfied and the probe beam will be absorbed by the medium. The prospect of the scheme working for single-photons hinges on the fact that the EIT linewidth should be as narrow as possible, implying that the ground-state decoherence should be smaller than the light shift due to a single photon. Additionally, the intensity of the single-photon needs to be focused down to a small mode area. The higher the optical depth of the medium, the higher the probability of absorption of this single-photon and higher the efficiency of the switch.

Another scheme that could find use in quantum computation is the 4-level scheme as proposed by Schmidt and Imamoglu [27] (see Fig. 2.5). This scheme

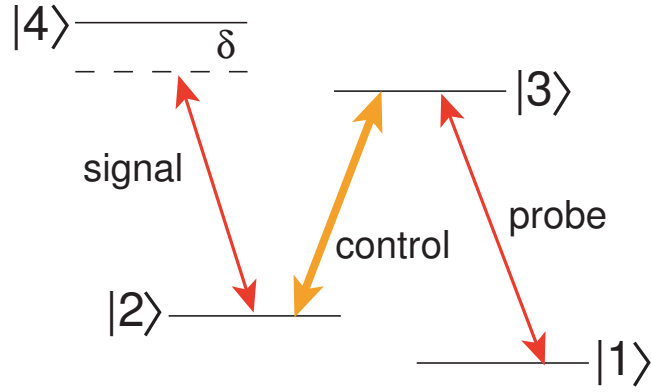


Figure 2.5: A 4-level cross-phase modulation scheme where the phase induced on a weak probe beam tuned on $|1\rangle \rightarrow |3\rangle$ transition is determined by the presence or absence of a very weak, ideally a single-photon signal tuned near the $|2\rangle \rightarrow |4\rangle$ resonance. This conditional phase imparted on the probe beam finds various applications in quantum phase gates and quantum non-demolition measurements of single-photons.

has the same 4-level system at its heart, but instead of using the imaginary part of $\chi^{(3)}$ as used by the switching scheme above, this scheme uses the real part i.e. the cross phase modulation. The signal beam is tuned off-resonance from the 2-4 transition, which ensures that the beam undergoes no linear absorption. Additionally, all self-phase modulations in the system are cancelled leaving only phase-shifts due to cross-phase modulation (XPM). Solving the coupled amplitude equations we find that the induced XPM

$$\Phi_{XPM} = \frac{\delta}{\Gamma_4} \alpha L, \quad (2.14)$$

where Γ_4 is the decay rate out of level $|4\rangle$ and αL is the optical depth of the medium. Here we really see how geometric enhancements can induce large phase shifts due to very high optical depths. Inducing a π phase shift is the basic requirement of quantum phase gates and can become an integral part of a quan-

tum computation architecture. Also, the possibility of detecting single-photons without destroying them can be crucial for use in quantum communication systems.

We see that EIT-based nonlinear optics schemes which are geometrically enhanced using the confinement of optical modes in waveguides and performed in atomic vapors that provide us with the requisite energy level structure and strong atom-photon coupling constants, show great promise for fulfilling the stringent requirements of performing single-photon nonlinear optics.

CHAPTER 3

WORKING WITH RUBIDIUM VAPOR: CHALLENGES AND TECHNIQUES

Soon after the invention of hollow-core photonic band-gap fibers, a whole host of experiments were proposed and implemented for performing nonlinear optics with lower power thresholds [13]. HC-PBGFs have been used in conjunction with molecular gases to show enhanced Raman scattering in hydrogen [28, 29], electromagnetically induced transparency with acetylene [30, 31], soliton generation with xenon [32], and as optical tweezers for levitating polystyrene spheres and guiding them through the core in air [33] and through liquid media [34]. However up until now, the ability to inject alkali vapors into HC-PBGFs has eluded researchers due to their strong reactivity towards the silica walls of the fiber. In this chapter¹, we shall describe the techniques used to overcome the challenges of working with rubidium. We also report the first-ever generation of Rb vapor inside HC-PBGFs and its use for performing nonlinear optics with nanowatts of power.

Alkali atoms are group 1A elements of the periodic table with a single electron in the outermost shell. All alkali atoms have full or nearly full inner shells which significantly shield the outer electron from the nucleus i.e. atomic electric field is small, which in turn results in the atom having a loosely bound outermost electron which can readily be lost in a chemical reaction, or is easily polarizable under the action of external fields. We know that whenever the external electric field approaches the atomic electric field, the nonlinearities contribute significantly to the optical response of the medium [15]. Thus the same proper-

¹Previous work to which the author made significant contributions: *Phys. Rev. Lett.* **97**, 023603 (2006)

ties which make alkali atoms interact strongly with light fields also make them highly reactive elements. The availability of photonic band-gaps in HC-PBGFs in the 800 nm region which completely support both the resonant D_1 and D_2 wavelengths of rubidium (Rb) makes the choice of the alkali atom and the fiber obvious.

3.1 Rubidium

Rubidium is naturally available in 2 stable isotopic forms - ^{87}Rb and ^{85}Rb in the ratio 28% and 72% respectively. The energy level diagram for Rb is shown in Fig. 3.1.

The ground state is hyperfine split and the two levels are not dipole-coupled to each other due to selection rule considerations [35]. The excited states are dipole coupled such that a transition with $\Delta F = 0, \pm 1$ is dipole-allowed (see Fig. 3.1). At room temperature, an equal proportion of atoms are found in the two ground states. Rb has a melting point of 40 °C and displays significant vapor pressure at room temperature ($\sim 10^{-6}$ torr at 33 °C) which makes it very easy to generate large vapor densities of Rb at modest temperatures. The reactivity of Rb makes handling it in vapor form challenging and ultrahigh vacuum (UHV) systems with very low oxygen levels are a must. In order to inject a vapor of Rb into a HC-PBGF, the entire mechanism for generating a Rb vapor, the fiber and fiber holders are required to be inside the UHV chambers the design of which will be described in the next section.

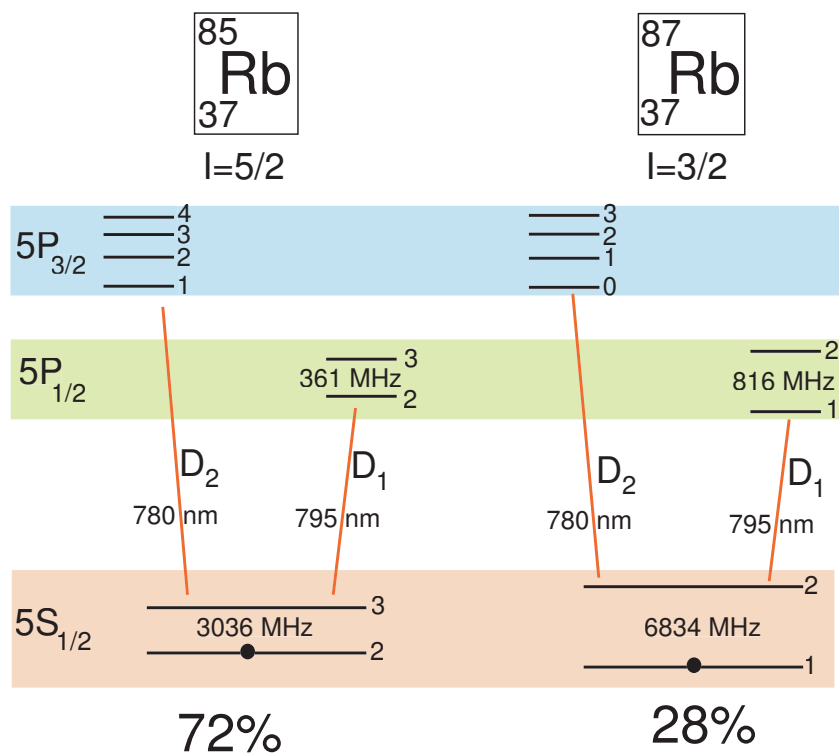


Figure 3.1: Energy level diagrams for the ground and excited states of ^{87}Rb and ^{85}Rb for the D_1 and D_2 transitions. The Rb nuclei have a nuclear magnetic spin denoted by I , and hyperfine coupling with the nuclear spin causes the ground and excited state to split into various hyperfine levels [35] denoted by the new quantum number F , which is noted on the right side of each energy level. The hyperfine splitting is noted for all levels except the $5P_{3/2}$ level for clarity, but can be found in the compilation by Steck [36]. Also the natural abundance is noted at the bottom.

3.2 The UHV system assembly

The primary challenge for creating a useful vapor of Rb atoms is the reactivity of the atoms with any available electron acceptor. Studies have shown that as soon as a vapor of Rb is generated in a vapor cell, the Rb vapor acts as a non-ideal sticky gas and the atoms attach themselves to the surface of the cell chemically by reacting with every available adsorbed oxygen or water molecule as well

as any dangling OH^- bonds that are ubiquitous on very pure silica surfaces. This process is called the “ripening” of the cell and only after every possible reactive site is covered, the Rb atoms form a stable, ambient vapor of Rb [37]. To minimize the loss of Rb atoms to surfaces and to hasten the ripening process two things must be ensured: 1) the available surface area is the bare minimum possible and 2) before introducing Rb, the UHV chamber must be thoroughly cleaned using ultrasonication and then baked out for a few days to remove any residual oxygen and water molecules.

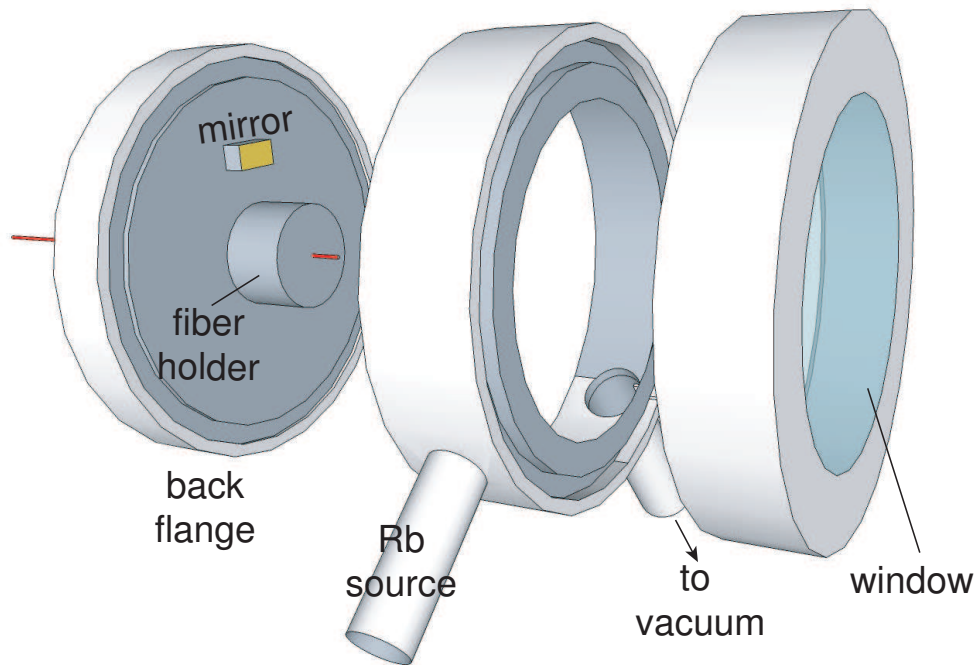


Figure 3.2: An exploded view of the vapor cell used for introducing Rb vapor into the hollow-core fiber (shown in red). The glass window enables light to be coupled into the fiber, while the middle flange provides connections to vacuum as well as the Rb source. A similar cell encloses the other end of the fiber.

To incorporate long fiber lengths (~ 30 cm) without having to ripen a large chamber, we decided to use a 2-cell design where only the open ends of the fiber

are maintained in UHV, while the rest of the fiber sits outside under 1 atm pressure. The cell design consists of commercially available stainless steel Conflat flanges which are modified via machining as shown in Fig. 3.2. A glass window in the front enables coupling light in and out of the fiber while the back flange has a hole drilled through to allow the fiber to enter the vacuum chamber via a Swagelok 1/4 in. two-ferrule tube fitting. The original design involved a machined PTFE ferrule [38] (inserted inside the Swagelok tube fitting) through which a no. 87 hole is drilled which is just large enough for the fiber to pass through. The PTFE ferrule deforms to make a vacuum-tight seal over the fiber jacket, which maintains good vacuum in the cell. This design was later replaced with steel ferrules forming a seal around a solid copper cylinder through which the fiber was passed into the cell. The gap between the no. 87 hole and the fiber is sealed with a UHV epoxy (Vacseal, SPI technologies). The middle flange provides mechanical support for the other 2 flanges as well as openings for Rb vapor and the vacuum connection to the pumps. The Rb source is just a steel appendage containing molten Rb which generates a steady vapor of Rb in the cell. The other cell is very similar to the one shown, except that it contains no Rb source. Both the cells are connected through a vacuum manifold to turbomolecular and ion pumps backed by a mechanical roughing pump. In order to maintain a uniform temperature over the entire length of the fiber so that Rb does not condense on cold spots and clog the fiber, the two cells are joined by a cylindrical oven like structure which is then kept at a constant temperature at least 10 – 15 °C above the Rb source (“the coldfinger”) using temperature regulated heating tapes. The Rb vapor density in the front cell is continuously monitored by bouncing a probe laser tuned to Rb resonances off a gold mirror attached to the back flange. The vapor density slowly increases as the cell ripens

and finally stabilizes to a value that depends on the temperature of the cell and the Rb coldfinger.

The atoms from the ambient Rb vapor in the front cell then start diffusing down the core of the fiber. For our fiber (AIR-6-800, Crystal Fibre A/S), the core is $6\ \mu\text{m}$ in diameter and is approximately 10^{-8} times smaller than the mean free path of Rb atoms at $60\ \text{°C}$. Since the surface area to volume ratio for the inside of the core of our fiber is very large, and we expect that the issues of chemical and physical adsorption on to the silica walls should be particularly severe. Additionally, those atoms that undergo collisions with the silica walls and remain in the beam suffer ground-state spin-decoherence [39]. For the fiber geometry, the rate at which the atoms collide ($> 50\ \text{MHz}$) could make the system impractical as a quantum device as discussed in the previous chapter.

The problem of collisions with the walls has been previously investigated in hot vapor cells and it was found that coating the cell walls with a layer of hydrocarbons such as paraffins or organosilanes significantly reduces the ground-state spin decoherence by four orders of magnitude as compared to bare silica walls [40, 41]. In spite of coating the cell walls, the high ratio of surface to volume ratio makes it challenging to generate and maintain a high density of Rb vapor in the volume of the core. Various methods for injecting atoms into the core such as dipole force based funnel beams [38] and light-induced drift based optical piston techniques [42, 43] were considered. Recently the phenomenon of light-induced atomic desorption (LIAD) [37, 44, 45] has been discovered in which alkali atoms adsorbed onto organic coatings are suddenly released on exposure to visible and near-infrared light in a non-thermal desorption process. Both these reasons make a compelling case towards attempting to coat the inner

core walls of the hollow-core fiber with organic coatings, which is challenging in itself.

For a core diameter of $6\ \mu\text{m}$, the process of coating a fiber with paraffin vapor leads to blocked capillaries which result in the loss of transmission and renders the fiber unusable. In order to maintain the band-gap of the fiber, we decided to pursue a wet chemistry approach to the problem of coating the core walls by chemically attaching a self-assembled monolayer of organosilanes [46] which forms exactly one layer of organic moieties. A schematic of the coating reaction is shown in Fig. 3.3(a) where a methanol molecule leaves as a byproduct while the 18-carbon chain long molecule is chemically attached to the silica matrix via hydrolysis forming a monolayer of organosilanes. The main advantages of this method are that the chemistry is simple and repeatable and after the coating procedure the fiber band-gap is preserved as shown in Fig. 3.3(b). Additionally, the coatings are robust and can withstand high temperature bakeout procedures ($200\ \text{°C}$) which are essential for creating a clean, oxygen and water free UHV system. The coating procedure protocols are discussed in Appendix A.

3.3 Experimental section

After the coating is completed, the fiber is attached to the two vacuum cells as shown in Fig. 3.4 and the entire system is baked at $200\ \text{°C}$ for a week after which the system is cooled to $65\ \text{°C}$. The fiber is then exposed to the Rb source which generates vapor at a pressure of 10^{-6} torr that ripens the front cell and diffuses down the fiber core. A weak probe beam ($< 1\ \text{nW}$) tuned to the D_1 transition of ^{87}Rb (see Fig. 3.5 inset) is coupled through the fiber to monitor the

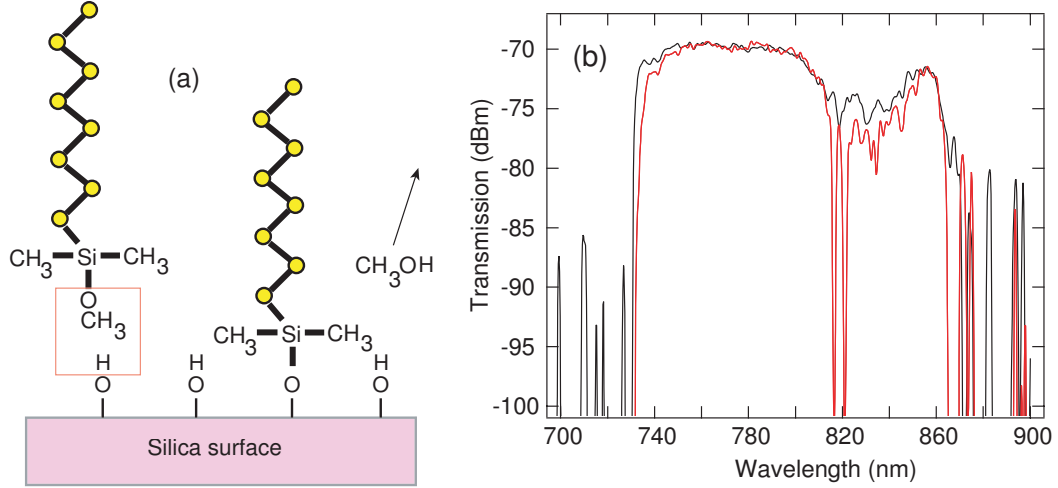


Figure 3.3: (a) The methoxy group of n-octadecyl dimethyl methoxysilane reacts with the dangling -OH bond on silica surfaces forming a self-assembled monolayer of the organosilane entities while a methanol molecule is released as a byproduct. (b) The band-gap obtained from fiber transmission measurements is essentially preserved on coating as shown by the data in red as opposed to the original band-gap as shown by the data in black.

Rb vapor in the core while a 1 mW desorption beam (770 nm) tuned far from any Rb resonances is coupled counter-propagating to the probe through the fiber. The absorption due to Rb atoms as seen through the fiber can be described by an ensemble of naturally broadened atoms (Lorentzian lineshape) distributed over the Doppler distribution (Gaussian lineshape). The resulting absorption lineshape $\alpha(\omega, \omega_0)$, called the Voigt profile, is a convolution of the Lorentzian over the Gaussian distribution

$$\alpha(\omega, \omega_0) = N_{atom} \int_{-\infty}^{\infty} \sigma(\omega, \omega_p) D(\omega_0, \omega_p, T) d\omega_p, \quad (3.1)$$

where ω is the frequency, ω_0 is the frequency at zero velocity, N_{atom} is the number density of atoms, σ is the atomic natural lineshape, D is the Doppler

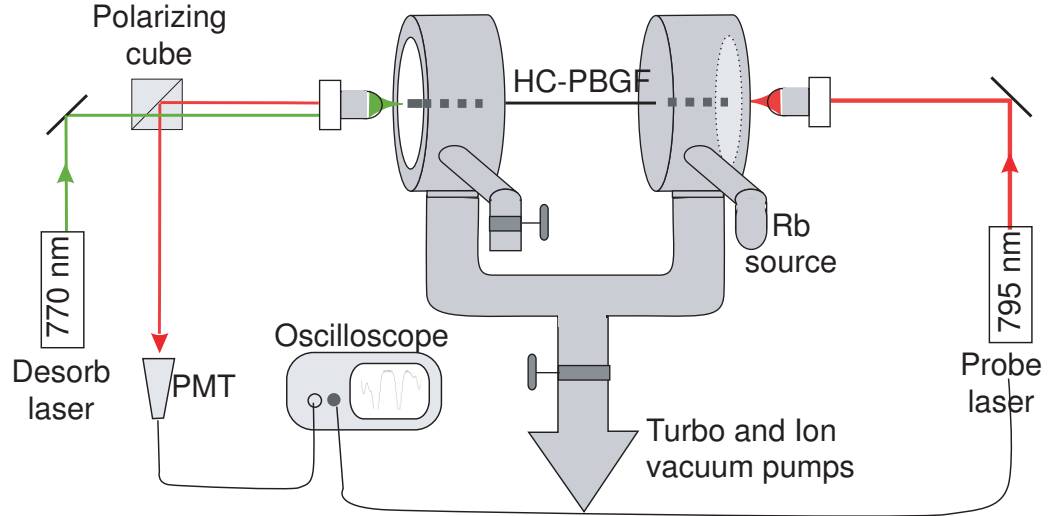


Figure 3.4: The experimental setup used to observe desorption. A 795 nm probe laser tuned to the D_1 line of ^{87}Rb is coupled through the fiber and detected using a PMT. A desorption laser tuned to 770 nm (far from Rb resonances) is coupled counter-propagating to the probe beam.

distribution which is a function of temperature T and ω_p is the variable over which the convolution is performed. Knowing the σ , one can extract N_{atom} values for a given temperature by fitting the calculated signal to the measured absorption profiles. Figure 3.5(b) shows the absorption through the fiber and the solid line shows the theoretical fit from which the number of atoms is extracted to be $\sim 2 \times 10^3$ atoms as shown in Fig. 3.5(a). When the desorption beam is turned on, we observe a significant increase in the atomic number as evidenced by the enhanced absorption over the entire Doppler lineshape. We estimate from the lineshape fits that the atomic number increases by almost 3 orders to 10^6 atoms. This is the first observation of LIAD inside hollow-core photonic band-gap fibers and gives a clear evidence that a significant vapor density of Rb can indeed be generated. The increase in atomic number is temporary and it decreases slowly with time as the adsorbed atoms get desorbed. Using a tem-

perature of 340 K, we get an estimated homogenous linewidth of 96 MHz, which remains approximately constant over 2 orders of atomic density variations, thus suggesting that collisions with the walls is probably the dominant decoherence mechanism as opposed to Rb-Rb self-pressure broadening interactions [47]. Estimating the rate of collisions with the walls as $\bar{v}/2r_{fib}$, where r_{fib} is the radius of the fiber = 3 μm and the \bar{v} is the average thermal velocity = 300 m/s, we get the collision rate to be ~ 50 MHz.

To demonstrate the potential of this system to facilitate nonlinear optics at low-light levels, we investigate EIT in a V -type system with a probe at 100 pW and with control powers as low as 10 nW; these control powers are 1000 times lower than what is typically used to achieve EIT in bulk geometries [48]. The probe is tuned to the $F = 2 \rightarrow F' = 1$ transition of the D_1 line of ^{87}Rb at 795 nm, and a control field, copropagating with the probe, is tuned to the $F = 2 \rightarrow F' = 3$ transition of the D_2 line at 780 nm. This wavelength difference of 15 nm makes it easier to separate the pump and probe using a dispersive element such as a prism, which would otherwise be difficult for co-propagating beams coupling out of the fiber in the same single-mode. This particular level scheme [inset of Fig. 3.6(b)] is chosen so that optical pumping between the hyperfine levels is avoided, since the $F = 1 \rightarrow F' = 3$ transition is dipole forbidden. Furthermore, the probe-field saturation and the optical pumping between the magnetic sub-levels tend to cancel each other, and as a result the observed transparency is primarily due to pure EIT [48]. To analyze this system, we solve the density-matrix equations for a 3-level V system in steady state, with level a as the ground state and with b and c as the two excited states [Fig. 3.6 (b)]. The coherence σ_{ca} to first order in the probe field is given by,

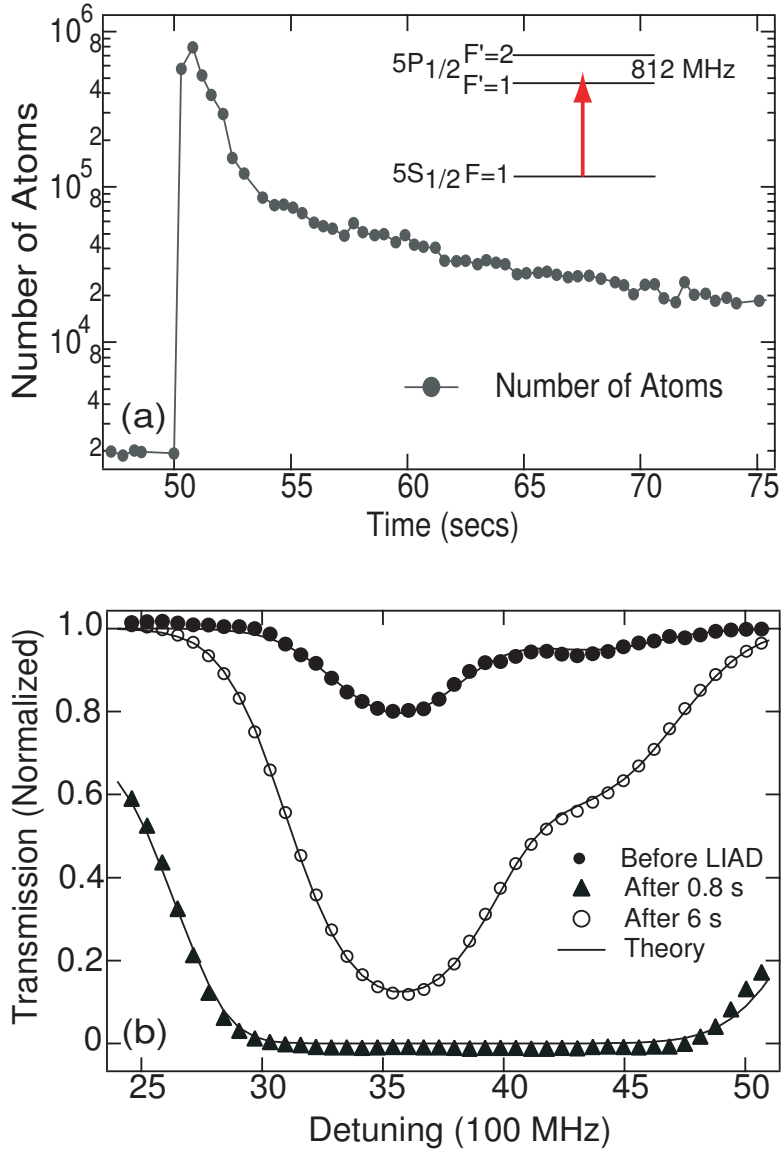


Figure 3.5: (a) Calculated number of atoms in the fiber core with the inset showing the energy levels being probed. (b) Normalized transmission showing the Doppler absorption features and the corresponding theoretical fits in solid lines.

$$\sigma_{ca} = \frac{-i\Omega_p}{2[\gamma_{ac} - i\delta_p + \frac{|\Omega_c|^2/4}{\gamma_{bc} + i(\delta_c - \delta_p)}]} \times \left\{ (\rho_{cc}^0 - \rho_{aa}^0) - \frac{|\Omega_c|^2(\rho_{bb}^0 - \rho_{aa}^0)}{4(\gamma_{bc} + i\delta_c)[\gamma_{bc} + i(\delta_c - \delta_p)]} \right\} \quad (3.2)$$

where Ω_c (Ω_p) and δ_c (δ_p) are the Rabi frequency and detuning, respectively,

for the control (probe) field, ρ_{ii}^0 , ($i = a, b, c$) are the steady-state population distributions, $\gamma_{ij} = (\gamma_i + \gamma_j)/2 + \gamma_{ij}^{coll}$, ($i, j = a, b, c$) are the dephasing rates, and γ_i is the decay rate of level i . The imaginary part of the Doppler-averaged susceptibility, calculated from this coherence, is integrated over the Doppler distribution over the length of the fiber to fit to the transmission trace of the probe field.

Figure 3.6 shows results in which a 1-mW desorbing beam releases Rb atoms into the core, and a series of probe transmission spectra are taken at ensuing time intervals. The time (250 ms) to obtain a trace is chosen to be long compared to the atomic time scales (100's ns) but short compared to the time scales (secs) associated with the desorption dynamics of the atomic density in the core. The input power of the probe field is set to 100 pW, and that of the control field is varied from 10 nW to 3 μ W. Figure 3.6(a) shows a typical trace of the probe field transmission in the presence of a 361-nW control field, together with the corresponding theoretical fit as calculated from Eq. 3.2. From the fit, we estimate a decay rate for the coherence between the two upper states to be $\gamma_{bc} = 24$ MHz and the two-level decoherence rates γ_{ai} , ($i = b, c$) to be between 90-100 MHz. As seen in Fig. 3.6(b), the measured transparency full-width at half maximum (FWHM) Γ_{EIT} is proportional to Ω_c at low powers and has a linear dependence on intensity at higher powers as is theoretically predicted [49]. At higher powers or for transitions in which optical pumping and saturation effects contribute, larger than 90% transparencies are observed [see inset of Fig. 3.6(a)].

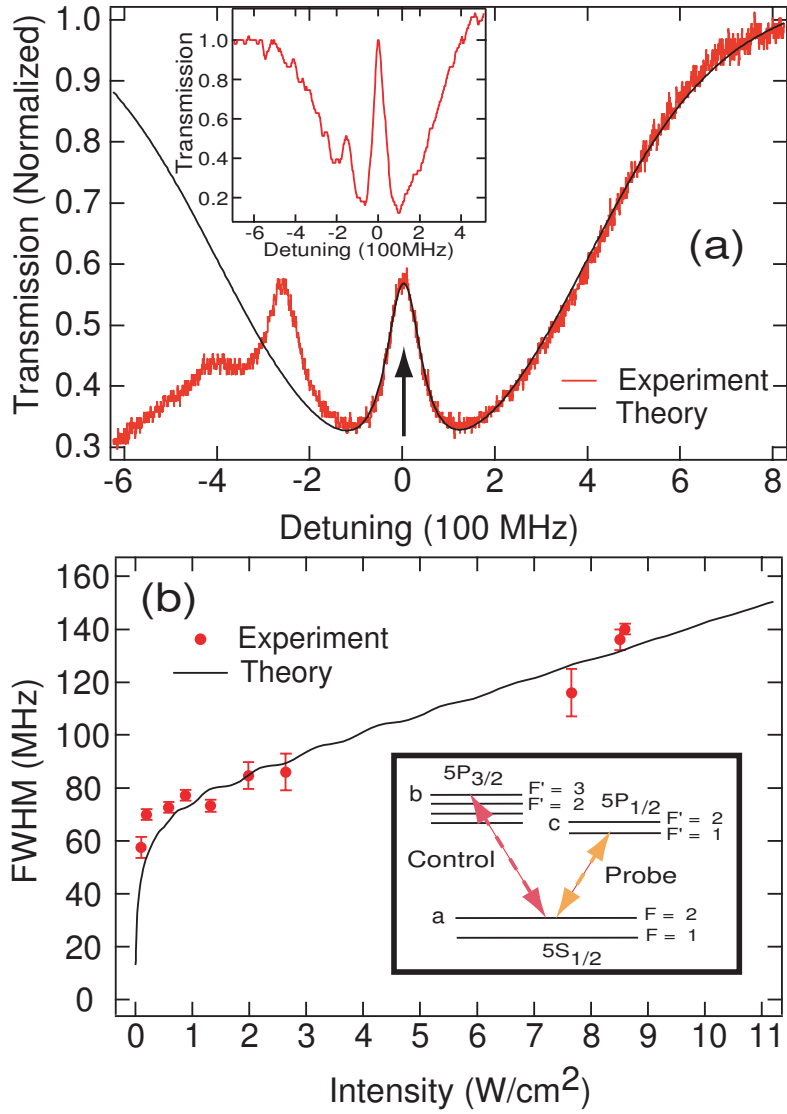


Figure 3.6: (a) Transmission spectra of the probe field in presence of a 361-nW control field. The arrow shows the transparency window due to electromagnetically-induced transparency (EIT) together with the corresponding theoretical fit. The peak to the left of the arrow corresponding to detuned $5S_{1/2}, F = 2 \rightarrow 5P_{3/2}, F' = 2$ transition is not taken into account in the fit. The inset shows transparency larger than 90% for a probe scanned over $5S_{1/2}, F = 1 \rightarrow 5P_{1/2}, F' = 1$ with a $2.65\text{-}\mu\text{W}$ control field tuned to $5S_{1/2}, F = 1 \rightarrow 5P_{3/2}, F' = 1$ transition. (b) Experimental (red) and theoretical (black) variation of the EIT linewidth as a function of the control intensity. The inset shows the energy-level scheme for this system.

3.4 Limitations of the setup and improvements

The above experiments have shown that it is possible to generate a significant density of Rb vapor inside the core of HC-PBGFs using LIAD. As a proof of concept, the generated vapor was successfully used for performing nonlinear optical effects such as EIT with very low control beam powers.

The measurements on EIT in the system have revealed that the wall collisional dephasing rate is quite high and the coatings do not seem to help with reducing the spin decoherence of the states involved in the coherent superposition. Perhaps, the few nm thick layer of coating is not thick enough to shield the Rb atoms from electromagnetic interactions with the silica surface, thus giving rise to spin decoherence. Moreover, the desorption signal gives us information about the number of atoms in the fiber, but we would like to understand how the Rb atoms are distributed along the length of the fiber.

As discussed in the previous section, desorption is performed with a strong, CW desorption beam. This has a number of drawbacks - the number of atoms generated cannot be exactly controlled and the entire reservoir of Rb atoms is exhausted in one shot. Once this reservoir is exhausted, we have found that the fiber does not desorb any more atoms and it takes 2 – 3 hours for the fiber to reload. If by some means the atoms can be released at the required amounts at high repetition rates, the system will gain immensely in terms of practicality. Additionally, the mechanisms responsible for dephasing of the atomic levels are dependent on the atomic velocities and we need to know the temperature of the desorbing atoms as they are released which is essential knowledge for further experiments involving cooling and trapping of atoms inside the fiber itself.

Thus, we need to understand the role of the organosilane coating in the desorption process as well as the mechanism of desorption in order to make the system more practical and feasible as a quantum optical device. Additionally, since the coatings do not mitigate the decoherence in the fiber geometry, we need to investigate other techniques to reduce the ground-state decoherence.

CHAPTER 4

GENERATION OF LARGE ALKALI VAPOR DENSITIES INSIDE BARE HOLLOW-CORE PHOTONIC BAND-GAP FIBERS

The demonstration of Rb vapor generation using light-induced atomic desorption inside hollow-core fibers coated with organosilanes begs to ask the question - what is the role of the coatings in the desorption process? Are the coatings essential for generating Rb vapor and what role do they play in the mitigation of ground-state decoherence in the fibers? Very recently, it has been reported [50] that alkali-atom desorption is possible from uncoated porous glass surfaces and that it may even be larger than that from hydrocarbon-coated glass. The thickness of the walls of the core as well as glass capillaries that form the photonic band-gap structure of the hollow-core fibers are tens of nanometers thick and as such could be expected to show similar behavior.

In this chapter¹, we present the first report of the large Rb densities that can be generated inside of an unmodified hollow-core PBGF by LIAD. We estimate on-resonance optical depths as high as 1200, which represents the generation of optical densities that are several orders of magnitude larger than have ever been reported for light-induced desorption [51]. The ability to use unmodified PBGF without the need for further chemical processing considerably simplifies this technology. Furthermore, we have found that such uncoated fibers show higher transmission properties and better-defined core modes than coated fibers, which allows for photonic interactions at even lower light powers.

¹A. R. Bhagwat[†], A. D. Slepko[†], V. Venkataraman, P. Londero and A. L. Gaeta, *Opt. Express* **16**, 18976 (2008) [†] These authors contributed equally.

4.1 The single-cell experimental setup

In order to investigate the effect of coatings on a fiber and to compare a coated and uncoated fiber with respect to each other, we need to modify the vacuum cell design. The coated and uncoated fibers need to be exposed to the same conditions of ambient vapor and temperature. Attaching long lengths (25 – 30 cm) of two fibers between 2 cells is technically challenging. Additionally, by choosing smaller lengths, we can observe the effects of fiber length on desorption performance of the fiber.

We assemble the PBGF Rb vapor cell by mounting two 4.5-cm-long (one coated, the other uncoated), $6\ \mu\text{m}$ core-diameter (Crystal Fiber Air-6-800) fibers inside a $2\frac{3}{4}$ in. diameter \times 2 in. length steel cell with glass windows attached to an ultrahigh vacuum station. A source of molten Rb is attached to the sample cell, as shown in Fig. 4.1. As before, the ambient rubidium vapor density is controlled by varying the temperature of the cell and the cold-finger assembly and is monitored by a laser beam resonant on the Rb D_1 transition, passing through the cell without coupling into the fiber. Light is coupled through the vacuum cell windows into the fiber core with a $10\times$ microscope objective located external to the vacuum assembly and is routed on transmission to a photomultiplier tube (PMT) for measurement. Part of the probe beam is sent to a CCD camera that images the front face of the fiber to assure coupling to the core mode which is necessary for short lengths of fiber. The desorption beam is obtained from a CW Ti:sapphire ring laser at 805 nm and is coupled counter-propagating to the probe, to reduce background light on the PMT. Typical transmission through a fiber-cell system with a pristine (non-Rb-exposed) fiber is 35 – 40%, which includes losses at the objectives and at the vacuum cell windows and due to fiber

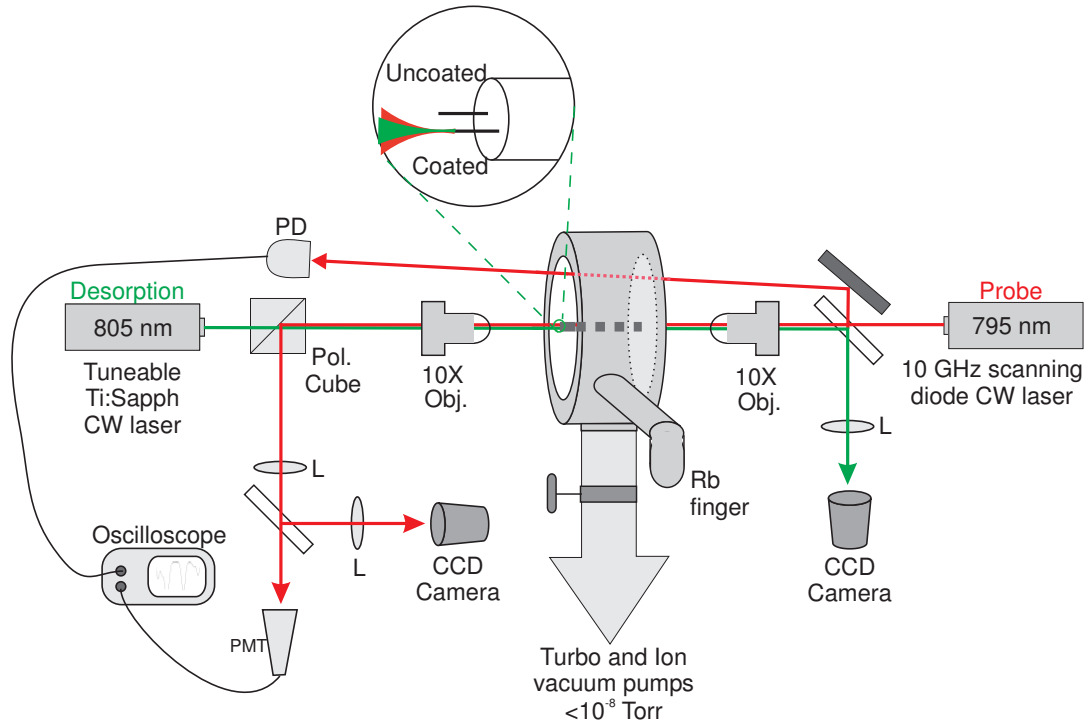


Figure 4.1: Two 4.5-cm-long hollow-core photonic bandgap fibers – one coated and the other uncoated are mounted inside a steel chamber with glass windows connected to an ultrahigh vacuum system. A 795-nm probe and 805-nm desorption beam are coupled into the fiber in counter-propagating geometry with 10× microscope objectives, and the coupling is monitored using a CCD camera. The probe beam can alternately be passed through the cell and detected by a photodiode to monitor the ambient cell Rb density. The coupled probe light is detected with photomultiplier tube (PMT). L: lens; PD: photodiode.

coupling. We typically use under 10 nW of transmitted probe power and 20 – 90 mW of incident desorption beam power.

Since transporting a fiber from atmospheric pressures into a UHV chamber is unnecessary, the vacuum obtained in this setup is better than the two cell setup. The ripening process is quicker and takes 2 weeks, after which a steady vapor of 4×10^{-6} torr is achieved in the cell. In this chapter we will primarily

deal with studies on the uncoated fiber, whereas the next chapter will deal with comparative studies.

4.2 Temperature measurement of desorbed Rb atoms

Figure 4.2(b) shows the first observation of LIAD from an uncoated fiber showing that coating the fiber is not essential for observation of atomic desorption from fibers. The probe is tuned to the $F = 2 \rightarrow F' = 2, 3$ transition of the D_1 line of ^{85}Rb . We illustrate a significant difference between optical interactions with the ambient Rb density in the vapor cell (shown in Fig. 4.2(a)) and the Rb that is generated from, and confined to, the fiber. We desorb a small amount of Rb within the fiber to roughly match the optical depth seen in the ambient vapor. The absorption lines fit well to Voigt profiles that account for both the homogeneous (Lorentzian) and inhomogeneously Doppler-broadened (Gaussian) lineshapes.

As shown in Fig. 4.2, the absorption profile of the fiber-borne Rb is considerably wider than that of the ambient Rb vapor. Fitting the in-cell Rb absorption lines to a Voigt profile that assumes a 5.75 MHz natural linewidth [52] yields a FWHM Doppler width of 570 MHz, corresponding to a cell temperature of 380 ± 30 K. In this case, the natural linewidth is overshadowed by the Doppler-broadened linewidth. The confinement of hot Rb atoms to the 6 μm -diameter core introduces a significant contribution of transit-time broadening. From a conceptual perspective, the absorption of probe power can only take place on average during the time it takes for hot Rb atoms to traverse the light mode. Limiting light-matter interactions to this timescale effectively broadens the ab-

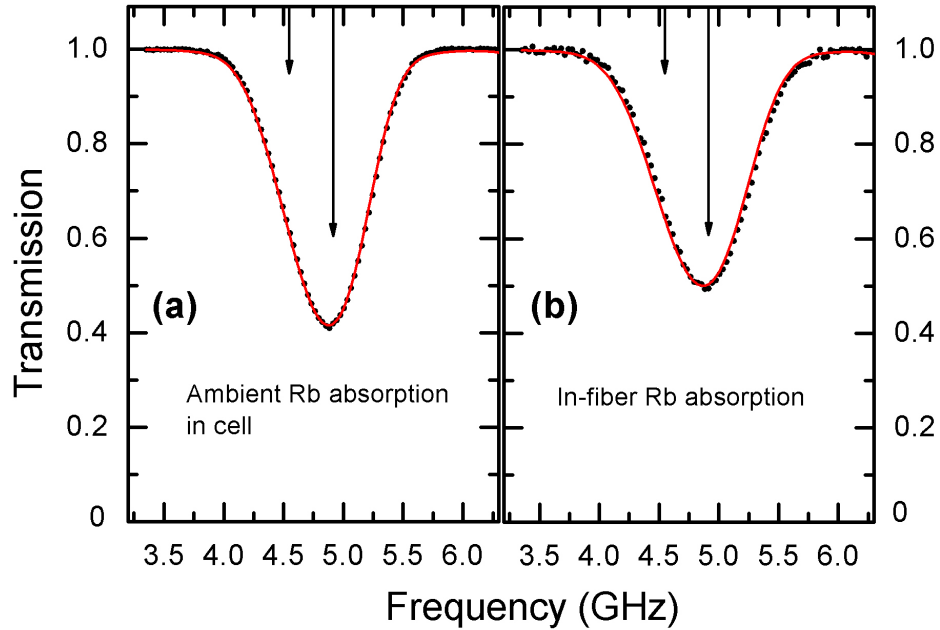


Figure 4.2: Absorption profiles of $F = 2 \rightarrow F' = 2, 3$ transitions in the D_1 line of ^{85}Rb . (a) The absorption profile of the ambient Rb vapor used to load the hollow-core fiber, as seen by passing light adjacent to the fiber. The position and relative oscillator strengths of the two transitions are indicated by the black arrows. The data is fit (black line) with a Voigt profile that assumes a natural linewidth of 5.75 MHz and yields a FWHM Doppler width of 575 MHz. (b) The through-fiber absorption profile in the presence of weak Rb desorption. The solid line is a fit to a Voigt profile with a Lorentzian component linewidth of 20 MHz, corresponding to transit-time broadening, and to a Doppler-broadening Gaussian component with a FWHM of 670 MHz. The key feature of note is that the through-fiber absorption profile is considerably broader than that of the ambient Rb vapor.

sorption lines, which is known as transit-time broadening [47]. However, under the unique conditions and geometries of hollow-core optical waveguides, transit-time broadening is on the order of tens of MHz [53] and can significantly contribute to Doppler-broadened absorption lineshapes. Estimating the transit-time of a hot vapor traversing a Gaussian optical mode, the Lorentzian

linewidth broadening is given by [54]

$$\Gamma_{tt} = \frac{0.58}{\pi} \frac{\bar{u}}{r_{1/e}} = \frac{0.58}{\pi r_{1/e}} \sqrt{\frac{2k_B T}{m}}, \quad (4.1)$$

where \bar{u} is the average velocity of the Rb atoms, $r_{1/e}$ is the light-mode radius, T is the temperature in kelvin, k_B is the Boltzmann constant, and m is the atomic weight. Approximating $r_{1/e} \sim 3 \mu\text{m}$ and $T \sim 500 \text{ K}$ yields a transit-time broadening of $\Gamma_{tt} \sim 20 \text{ MHz}$. Since the Doppler width also scales as $T^{1/2}$, the two are correlated, and we can fit the in-fiber absorption profile to a Voigt function, where only temperature and the number of atoms are the free parameters. Doing so, we obtain a fit that yields a temperature of $520 \pm 40 \text{ K}$ for desorbed Rb atoms in the PBGF. Comparing this with our obtained temperature of $380 \pm 30 \text{ K}$ from fits to the ambient Rb absorption profiles from the front cell [Fig. 4.2(a)], our data conclusively indicates that the Rb atoms desorbing from the glass core are hotter than the ambient temperature. Because of the transient nature of the Rb vapor density, this apparent temperature represents the kinetic energy of the Rb vapor, and does not necessarily reflect a thermally-equilibrated fiber temperature.

Thus, because the ambient Rb vapor and fiber-confined vapor behave differently, we examine the possibility of removing the ambient Rb density once the fiber has been “loading” for a few weeks, which guarantees that any Rb in the system is wholly fiber borne. This protocol has a further added operational advantage: The primary failure mechanism of our cells over the course of months to a year has been the cracking of the cell windows where it is continually exposed over a long period of time to the corrosive Rb vapor. Thus, the ability to operate such cells with only intermittent periods of ambient Rb-glass window

interactions is expected to drastically increase the lifetime of fiber-based vapor cells.

We have studied the generation of Rb by LIAD in such a pre-loaded fiber. Rb is loaded into the fiber by exposing it to ambient Rb vapor at 70 °C for 3 weeks. Regular desorption seems to help quicken the process, probably due to the fact that desorbing the atoms increases the possibility of the atoms making it further down the length of the fiber and longer lengths imply enhanced desorption. Once the fiber demonstrates strong light-induced desorption, the temperature is reduced to 20 °C, thereby removing the ambient Rb vapor density by two orders of magnitude to about 1×10^{-7} torr, and below our measurement resolution. Even in the absence of constant Rb-loading, we observe a strong LIAD signal. To the best of our knowledge, the amount of Rb generated in the fiber in-vacuo is on the same order as that generated in the presence of constant Rb-loading. We have used this fiber daily for weeks, over a wide range of desorption cycles. We have observed that while the total amount of available (desorbable) rubidium in a pre-loaded fiber decreases with use, the near instantaneous densities of vapor generated with a strong desorption pulse (40 – 60 mW) remains nonetheless very large at least for a few weeks (on the order of fifty such 1 – 20 s long desorption events).

We now turn up the desorption beam power and measure the optical depth generated as a function of power. Fig. 4.3 shows absorption profiles from Rb density generated in a pre-loaded fiber. The profiles of three different Rb densities are shown. It is difficult to estimate with certainty the optical depths at high Rb densities. At optical depths greater than 4, there is insufficient transmission on resonance to directly measure the extinction with a standard photodetector.

A suitable technique to estimate optical depth from the absorption profile is to fit the transmission trace to a set of Voigt profiles, where most of the information regarding the vapor density lies in the wings and rising slopes between resonances. There are six natural Rb resonances within the investigated spectral range. We fit a linear superposition of integrated Voigt profiles of six of the Rb lines weighted by their abundance, oscillator strengths, and degeneracy, as shown in Fig. 4.3. The temperature of the Maxwell-Boltzmann distribution and an absorption pre-factor are freely varying parameters that are used to optimize the fit to the observed data. By comparing the absorption pre-factor to a standard pre-factor that generates an optical depth of 1 at the highest absorption point (between $^{85}\text{Rb } F=2 \rightarrow F'=2,3$), we deduce the optical depth as seen through the fiber. A temperature-dependent transit-time broadening (see Eq. 4.1) is also included in the Lorentzian linewidth as part of the Voigt profile.

At lower optical depths, as shown in Figs. 4.3(a) and (b), the fits yield a temperature of 505 ± 30 K. Depending on the timing and length of the desorption pulse, a wide range of optical depths can be produced. Figure 4.3(b) shows an absorption profile for a moderate Rb density. Here, the maximum optical depth (OD) is defined as

$$OD = -\ln T(\nu)_{min}, \quad (4.2)$$

where $T(\nu)_{min} \sim e^{-47}$ is the minimum transmission. When the intense desorption beam is first turned on, a large Rb density is generated within a few milliseconds. As seen in Fig. 4.3(c), sufficient Rb density is created to give near complete absorption across the entire D_1 line.

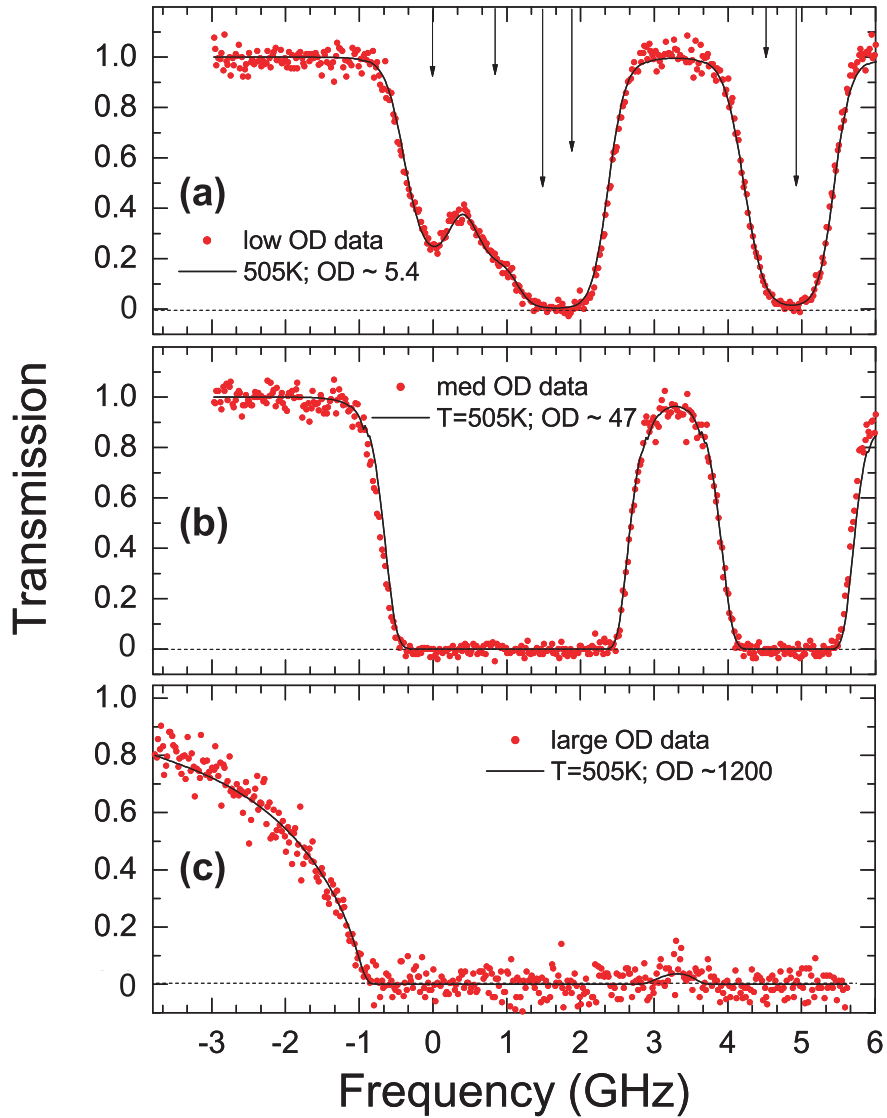


Figure 4.3: Absorption profiles of lines in the D_1 transition of ^{87}Rb and ^{85}Rb . The frequency scale is zeroed on the lowest energy D_1 transition (^{87}Rb $F=2 \rightarrow F'=2$). (a) A relatively low optical depth of Rb. The black line is a fit to six Voigt lines that include the effects of transit-time broadening (see text). The position and relative absorption strength [52] are represented by the black arrows and their lengths, respectively. (b) A moderately high optical depth generated by LIAD with black line as a free fit to the data. (c) The absorption profile of a large density, with a conservatively estimated optical depth of ~ 1200 between the $F=3 \rightarrow F'=2,3$ resonances of ^{85}Rb .

Estimating the optical depth of the largest Rb densities we can generate by LIAD is complicated by the fact that at such a large atomic density and desorption beam intensity, additional broadening mechanisms such as collisions with other Rb atoms and light-shifts may be present, which further complicates the absorption lineshapes. The best indication of the optical depth lies in the fact that the region between the ^{85}Rb $F=3 \rightarrow F'=3$ and ^{85}Rb $F=2 \rightarrow F'=2$ lines (at a detuning of 3.3 GHz) experiences almost complete absorption. In an attempt to estimate the optical depth implied by the absorption presented in Fig. 4.3(c), we use the fitting parameters obtained from fits to the low-to-moderate OD absorption data, and further assume a $\sim 5\%$ transmission peak at 3.3 GHz. We thus estimate that the optical depth of the absorption profile shown in Fig. 4.3(c) to be approximately 1200. It is possible for such rapid generation of Rb density at the onset of desorption that the atoms are considerably hotter than the estimated 500 K. While we have no indication that this occurs, in such a case the OD would be significantly lower than our estimates.

A comparison between a hollow-core fiber based vapor cell and a standard glass vapor cell demonstrates several key advantages to a fiber-based device: The primary advantage lies in an ability to dynamically and rapidly modulate the optical depth. Our demonstration of the ability to generate ODs between 0 and 1000 within a few seconds is unique. Furthermore, because the desired Rb densities in standard vapor cells are obtained thermally, the absorption profile is ever-changing due to increasing Doppler widths. Thus it is impossible to dynamically change the optical depth in a standard cell without changing the spectral profile. As the data in Figs. 4.3(a) and (b) show, we can achieve large increases in optical depth without corresponding temperature changes. Thus, this type of vapor cell may find application as an isotopically-pure filter cell [55]

where, for example, the fiber is loaded with pure ^{85}Rb and buffer gas, and a sufficiently high Rb density is generated by LIAD such that a large optical depth is obtained 1.6 GHz from the line centre, but no absorption is present at 1.9 GHz. This would act to completely filter out one of the ^{87}Rb D_1 doublets ($F=2 \rightarrow F'=1,2$), while passing the other ($F=1 \rightarrow F'=1,2$).

Another major advantage of our cell geometry is an expected abatement of radiation trapping effects [56]. Radiation trapping occurs in optically dense media when spontaneous fluorescence is absorbed by ground-state atoms before it can escape (or be detected). This effect is exacerbated in media with a large transverse-to-axial density ratio. Our geometry, wherein the aspect ratio of transverse-to-axial lengths is < 5000 and where the interaction region (light mode area) essentially fills the entire transverse extent of the vapor is ideal for minimizing radiation trapping. Thus, the hollow-core PBGF vapor cell may be uniquely suited for quantum nonlinear optical experiments where dynamically varying and large optical depths are needed, but where radiation trapping is a concern.

4.3 Conclusion

We have demonstrated strong light-induced atomic desorption of Rb atoms in uncoated, hollow-core PBGFs. Previously, LIAD was thought to be possible only from fibers that have been microfluidically-treated with hydrocarbons [57]. Thus, the discovery that desorption in a bare fiber can generate at least as much Rb as has been seen in a coated fiber, is significant, since it considerably simplifies their use. We show that the absorption profiles of the ambient cell Rb

and fiber-borne Rb densities to be distinct, demonstrating that the in-fiber absorption profile is wider due to transit-time broadening and due to atoms desorbing at temperatures higher than the walls. Subsequently, we have found that once the fiber is exposed to Rb vapor at 50 - 100 °C for a few weeks, the ambient rubidium may be removed and the fiber can be repeatedly used for an extended period of time in-vacuo. Such a fiber can generate large optical depths, estimated to exceed 1000 on the ^{85}Rb D_1 resonance. One of the uses of such a fiber-based vapor cell for optical filtering of particular hyperfine levels and for sensitive quantum nonlinear optical measurements where large optical depths are needed and where radiation trapping must be minimized.

CHAPTER 5
ON-DEMAND ALL-OPTICAL GENERATION OF CONTROLLED
RB-VAPOR DENSITIES IN PHOTONIC BANDGAP FIBERS

5.1 Introduction

In the previous chapters we described the use of a HC-PBGF-based geometry for demonstrating coherent atom-photon interactions with Rb vapor at ultra-low-light control powers [57]. The fiber walls were coated with a self-assembled monolayer of organosilanes [n-octadecyl dimethyl methoxysilane (ODMS)] in order to prevent the Rb atoms from reacting with the walls and to reduce the effects of spin decoherence from collisions with the wall [40, 41]. The technique of light-induced atomic desorption (LIAD) [37, 44, 45] was then used to generate a large population of Rb atoms inside the hollow core. Furthermore, we showed that the coatings are not essential for the desorption process to work and we can generate very high optical depths using only an untreated fiber.

In this chapter¹, the time-dynamics of light-induced atomic desorption in hollow-core photonic bandgap fibers are studied using a pulsed desorption scheme to investigate the viability of controlled high-repetition-rate generation of Rb-vapor. By comparing coated and uncoated fibers under identical conditions, we show that coating the fibers does not affect the desorption mechanism which, furthermore, shows two distinct time signatures. We also investigate how the capacity for desorption from the fiber recovers as a function of time after the fiber has been completely desorbed and propose a mechanism to ex-

¹A. R. Bhagwat, A. D. Slepko, V. Venkataraman, P. Londero and A. L. Gaeta, *Phys. Rev. A* **79**, 063809 (2009)

plain the desorption process based on our observations. Lastly, we observe a Rb vapor which persists after switching off the desorption beam, which we further use to demonstrate Λ -scheme EIT.

5.2 Experimental Setup

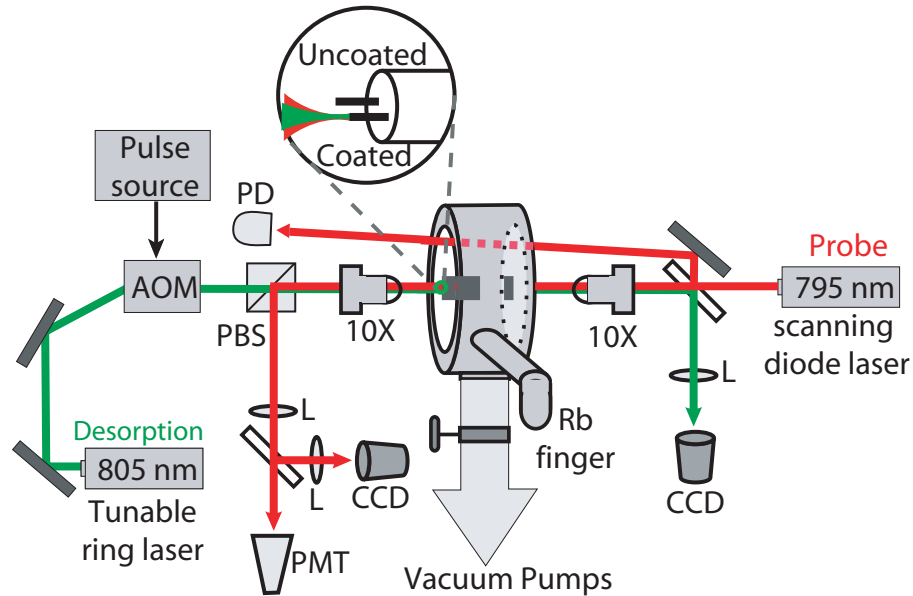


Figure 5.1: Two fibers: one coated and one uncoated (4.5 cm long) are placed inside a vacuum cell with glass windows on both sides. The desorption and probe lasers are coupled counter-propagating through a given fiber. A CCD camera is used to ascertain that the lasers are coupled to a single mode in the fiber core. A photodiode (PD) monitors the ambient Rb vapor density in the cell. PMT: photomultiplier tube, L: lens, PBS: polarizing beamsplitter, AOM: acousto-optic modulator

The experimental setup is essentially the same as discussed in chapter 4 (see Fig. 5.1) with two fibers exposed to the same vapor conditions and with counter-propagating probe and desorption beams. The power and duration of the desorption beam is controlled using an acousto-optic modulator (AOM) that varies

the amount of power coupled into the fiber. Using the AOM we generate desorption pulses as short as 100 ns to study the desorption process at various timescales. The probe beam is passed through narrow-band 795-nm filters (TFI 795MC10) and is detected using a PMT (Hamamatsu H7422-50). The output of the PMT is coupled to an oscilloscope using a suitable impedance termination (Thorlabs VT1). As before, we use CCD cameras to image the fiber end-face to monitor the mode of the light coupled into the fiber.

5.3 Effect of desorption on Fiber Transmission

Before exposure to Rb, the coated fiber exhibits a lower transmission (10-15%) than the uncoated one (25-30%) at 795 nm. This indicates that the coating perturbs the bandgap guidance of the fiber possibly due to increased scattering from the coating, although the actual bandgap is not seen to be altered significantly. The Rb atoms diffuse down the fiber core, are adsorbed on to the fiber walls, and diffuse transversely into the glass matrix facilitating further adsorption of Rb atoms on the surface. This ripening process of the fiber can be accelerated by desorbing regularly during the initial stages.

We have observed that this adsorption process increases the scattering inside the fiber and reduces its light throughput and hence the fiber transmission. This can be observed in Fig. 5.2(a) where the scattered light leaks out into the fiber cladding. Exposing this fiber to a strong desorption beam not only desorbs the atoms but also increases the coupling of the desorption beam through the fiber. This generates a positive feedback wherein as the desorption beam coupling increases so does the rate of desorption, which increases the coupling further.

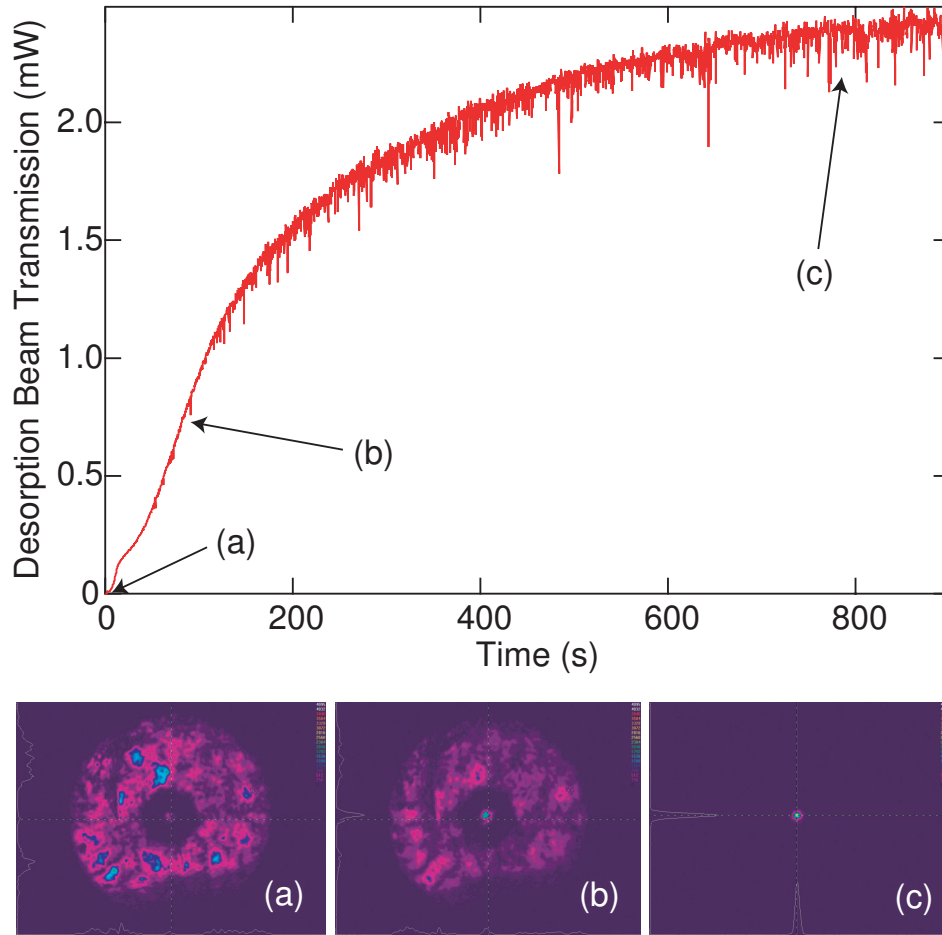


Figure 5.2: The transmission of the desorption beam shows a positive feedback behavior where as the coupling of the desorption beam increases more atoms get desorbed and the coupling improves further. The fiber end is imaged at various times as shown: (a) At the beginning, most of the light is scattered out and leaks into the cladding layer. (b) Coupling improves over time as more of the light is retained in the core. The image is taken with a neutral density filter of 2. (c) A fully desorbed fiber regains its single-mode coupling. The image taken is with an additional neutral density filter of 2.

Fig. 5.2(b) shows an intermediate stage of desorption, whereas Fig. 5.2(c) shows a fully desorbed fiber with light completely confined to a single core mode. For a fully ripened fiber, desorption can restore the transmission to 10% for a coated and 20% for an uncoated fiber at 795 nm.

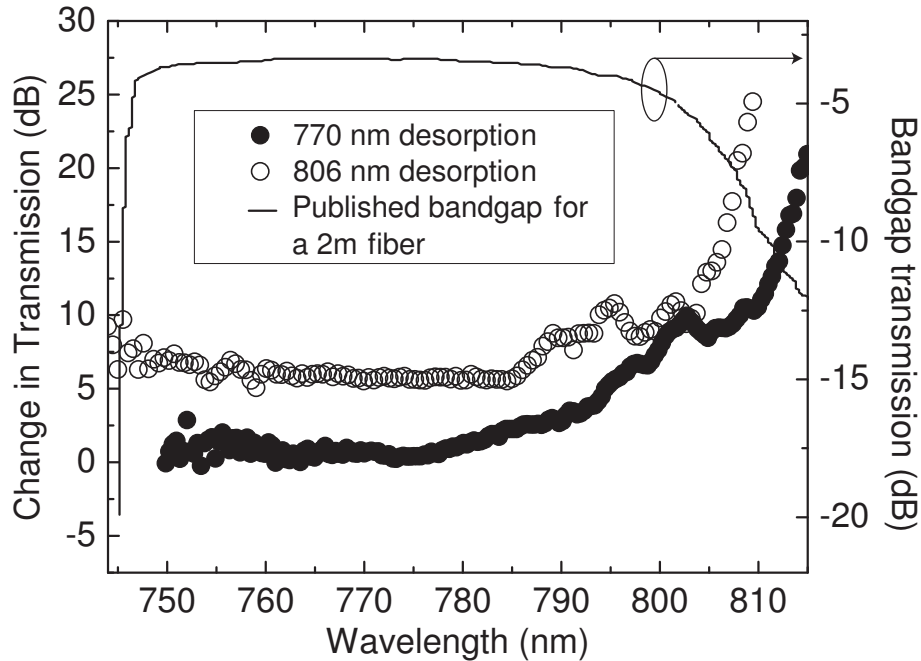


Figure 5.3: Change in spectral transmission of a broadband probe beam due to the desorption process for a coated photonic band-gap fiber over its entire band-gap. The data represented by open circles are for a 806-nm desorption beam while those shown by the solid circles represent data for 770-nm desorption beam. The solid line shows the published bandgap for a 2-m-long fiber and illustrates the band-edges [58]. Both sets of data show a larger increase in transmission at the higher wavelength band-edge. The data for an uncoated fiber follow similar trends (not shown).

The presence of adsorbed Rb atoms on the fiber walls changes the fiber transmission over its entire bandgap. Figure 5.3 shows the ratio of transmission before and after desorption over the entire bandgap for the coated fiber, which was probed using a broadband supercontinuum source. The increase in transmission is fairly uniform over the entire bandgap except at the higher wavelength edge. The possibility of the formation of nanoclusters of adsorbed atoms on porous silica surfaces which exhibit resonances based on their sizes has been recently suggested [59]. Such nanoclusters then undergo resonant heating and

vaporize, generating a Rb vapor. In order to probe the possibility that nanoclusters resonant around 810 nm were selectively vaporized, we shifted the desorption wavelength to 770 nm to probe size-based resonances and selectively desorb 770 nm resonant nanoclusters that should result in an enhanced transmission at that wavelength. As shown in Fig. 5.3, the change in transmission observed with 770 nm desorption beam is nearly identical to that with 806 nm. Size-based resonances having linewidths [60] greater than the fiber bandwidth cannot be distinguished clearly in the current setup, and it is possible that the fiber bandgap is blue-detuned from the peak wavelength of surface-plasmon resonances of Rb nanoclusters formed inside the fiber core, thus explaining the higher wavelength band-edge effects as well as the larger transmission change for 806 nm desorption beam.

5.4 Temporal dynamics of LIAD

We characterize the temporal dynamics of the desorption process by coupling desorption pulses of varying duration into the fibers. During the desorption process the transmission of the fibers increases steadily over time. Hence, we use the off-resonance transmission of the probe to characterize the transmission increase, and normalize the on-resonance transmission data to it to obtain absorption information purely due to Rb-vapor. When the fibers are exposed to 100- μ s desorption pulses, immediately after turning on the desorption pulse, the Rb vapor increases within 10 μ s and then slowly decays. Figure 5.4 shows the ratio of on- to off-resonance transmission indicating the absorption that is solely due to Rb-vapor. For a 10-ms pulse [see Fig. 5.4(a)], we observe the transmission to decrease slightly and then remain constant over the entire duration

of the pulse which indicates a steady generation of vapor. The time-dynamics of coated and uncoated fibers are essentially identical, and the coating may change the absolute amount of vapor produced but does not alter the dynamics of desorption. For a 1-s duration pulse, we observe that the OD remains steady for 50 ms after which a second desorption mechanism generates much higher vapor densities. This is manifested as a large decrease in on-resonance transmission despite the high off-resonance transmission (not shown), which indicates that Rb vapor is responsible for this absorption. As the absorption evolves further in time, we observe optical depths greater than 1000 in the fiber at longer time intervals [61].

After the desorption pulse is turned off, the off-resonance transmission is restored to its original value, but the on-resonance transmission remains low resulting in continued absorption [shown in Fig. 5.4(b)], which decreases slowly with time. We attribute the presence of this residual vapor to the fact that the amount of Rb population generated may be too high for complete immediate re-adsorption of the entire vapor. The fiber walls are saturated with adsorbed Rb atoms, and the main adsorption rate is governed by diffusion through the glass. It has been reported that the diffusion of alkali atoms through siloxane coatings can be modified by presence of light [45]. The limiting of adsorption rate in both coated and uncoated fibers suggests that fast light-induced diffusion of Rb out of the glass matrix and slow diffusion back into the glass could explain the behavior. The other possibility is that once the Rb nanoclusters get heated, they keep desorbing even after the desorption beam is switched off. The presence of residual vapor is advantageous for performing interactions with Rb vapor in the absence of any desorption beams, which can otherwise give rise to significant AC Stark shifts (> 10 MHz/mW) and increased scattering resulting

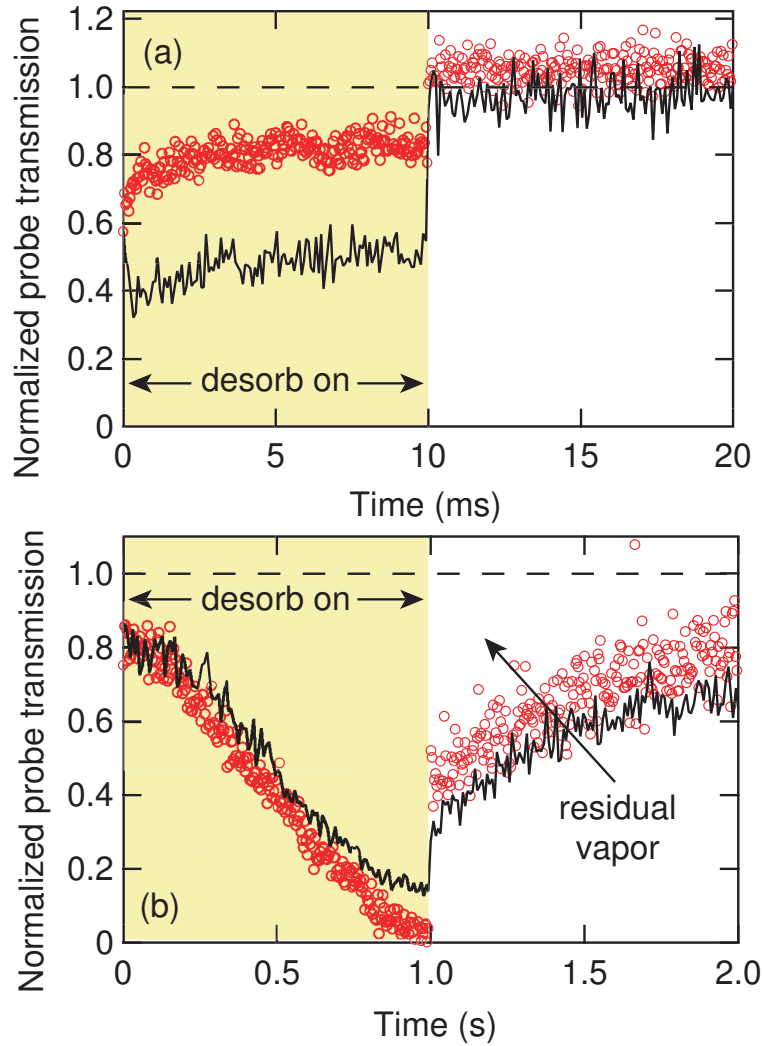


Figure 5.4: Desorption signature at two different timescales. The shaded area denotes the time for which desorption pulse is on, while the dashed line represents transmission in the absence of desorption. Data in red circles indicate transmission change in a coated fiber while the data in uncoated fiber are indicated by the black curve. The data have been corrected for fiber coupling changes due to desorption and only indicate the effect of Rb vapor absorption. Relatively low desorption powers (10-15 mW incident) are used to generate optical depths suitable for displaying time-dynamics with sufficient dynamic range.

in perturbation of sensitive measurements. In fact, we have successfully used the residual vapor to demonstrate EIT as described below.

After exposure to a strong CW desorption beam, the fiber is completely depleted and requires approximately 2 hours to recover before it can generate as much vapor as an undesorbed fiber. Does the vapor escape through the fiber ends? Does the fiber load up after every shot from the ambient vapor? To understand these questions, the Rb source and the cell are cooled down to room temperature. A probe beam is passed directly through the cell to ensure that there is no measurable Rb vapor in the cell ($< 10^{-7}$ torr). Surprisingly, we observe that the fibers require the same amount of time to recover irrespective of the presence of ambient vapor, and the fibers continue to desorb for weeks (with regular desorptions every 2 hours) after which they show a decrease in the generated Rb vapor. This shows that the Rb desorbed by the fiber is not in continuous equilibrium with the ambient vapor in the cell. Over a period of weeks, the atoms are lost either due to chemical means or through the fiber ends, which eventually results in a decrease in the generated vapor if no ambient vapor is present.

Figure 5.5 shows the recovery of this desorption capacity over short time periods. The fiber is exposed to 1-ms desorption pulses carved out of a 40 mW beam and is probed by a weak CW beam tuned to an ^{87}Rb D_1 transition. Initially, an undepleted fiber is exposed to a single 1-ms desorption pulse to measure the original desorption capacity. The fiber is then exposed to a train of consecutive pulses (> 30 at 50% duty cycle) till maximum depletion is achieved and the transmission is recorded (Fig. 5.5, time elapsed = 0). We then let the fiber recover in the dark and probe the density generated by a single 1-ms desorption pulse at different elapsed times. We observe both “fast” and “slow” mechanisms that produce a Rb vapor. As shown in Fig. 5.5, the fast mechanism produces a lower density of atoms, which peaks within a few μs and falls off and it is this mecha-

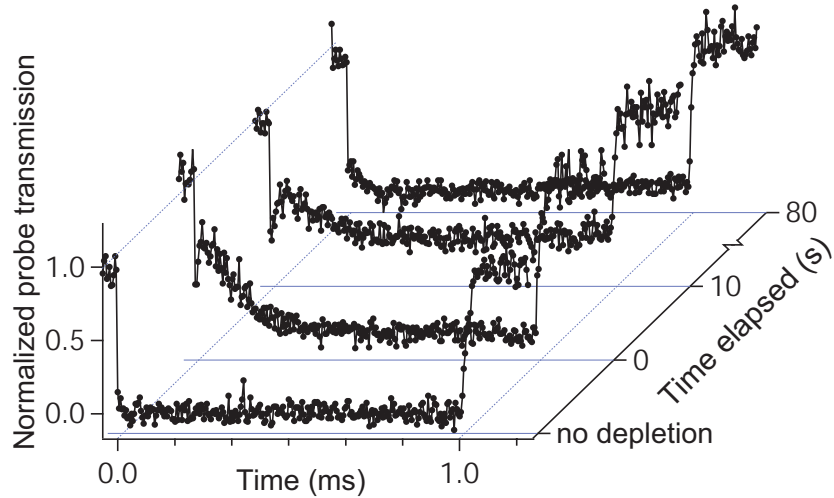


Figure 5.5: The recovery of the desorption capacity of an uncoated fiber is studied. A 1-ms desorption pulse generates almost complete absorption of probe on the first exposure. After repeated exposure of the fiber to many 1-ms desorption pulses, the probe absorption at the beginning of the pulse shows depletion and is maximally depleted at elapsed time = 0 s. The probe absorption is then recorded during exposure to identical 1-ms desorption pulses at subsequent time intervals, and we observe that the absorption slowly recovers to match its initial desorption capacity before depletion.

nism which shows a distinct recovery as a function of time elapsed between depletion and probing. The slow mechanism produces a larger Rb density which slowly increases over a period of hundreds of μs .

A second experiment is performed, where instead of a pulse train of 1-ms desorption pulses, we expose the fiber to a 2-s desorption pulse with the aim of significantly heating the nanoclusters and observing the recovery of the second, slower desorption mechanism. As shown in Fig. 5.6, the exposure to a 2-s desorption pulse causes the slower desorption mechanism to be depleted and the later end of the pulse shows reduced absorption. The fast mechanism depletes quickly and recovers quickly such that we do not see it change in this

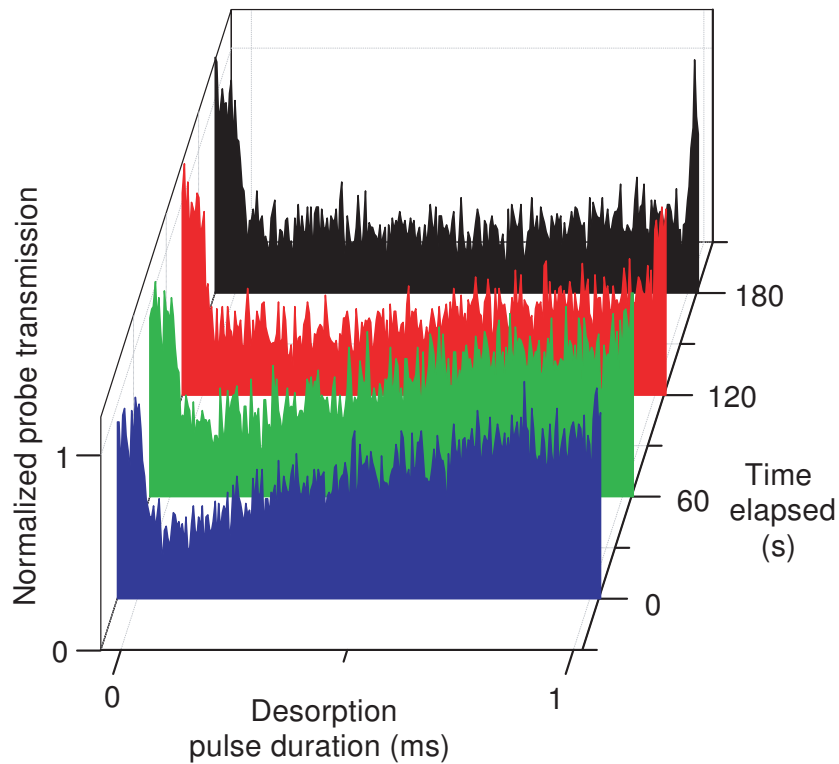


Figure 5.6: The fiber is initially exposed to a 2-s desorption pulse and its desorption capacity is then probed with 1-ms desorption pulses at various time intervals. We observe the absorption in the later part of the pulse to get depleted, while the initial part remains unchanged. The slower desorption recovers over the course of time as shown.

experiment. Instead of a 2-s pulse, if we let the fiber desorb for much longer time intervals (> 40 s), the slower desorption takes 2 hours instead of minutes to recover.

Based on the above observations, we present a model for the desorption mechanism in hollow-core fibers. We postulate that the Rb atoms can reside either 1) on the surface forming a contiguous metallic layer or non-contiguous agglomeration of nanoclusters or 2) diffused into the glass matrix. Over a period of time, the fiber can build up a significant reservoir of diffused Rb atoms

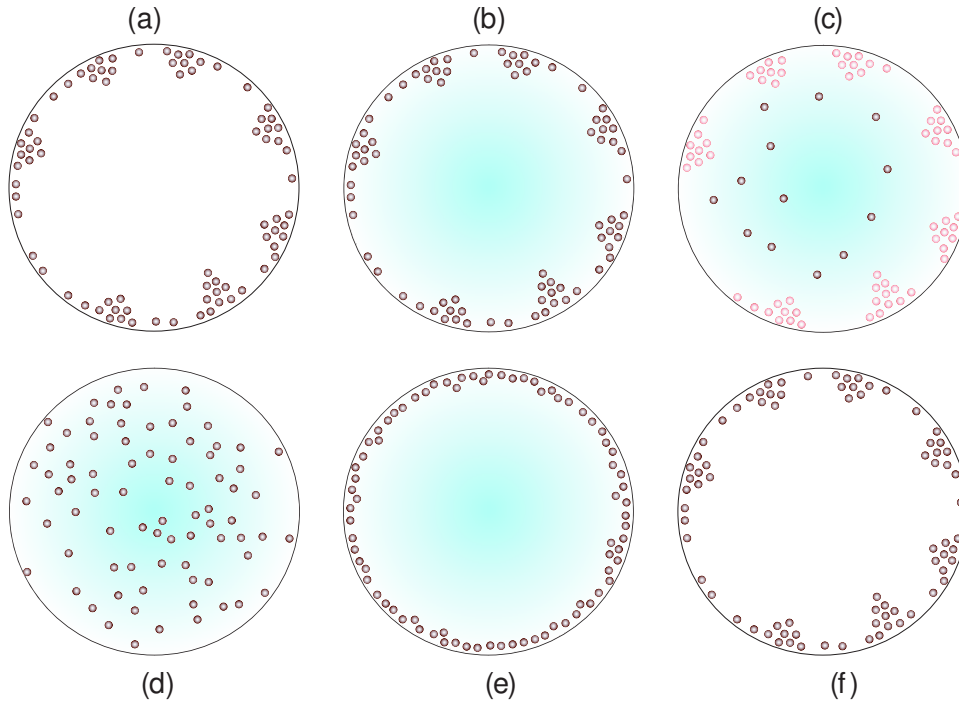


Figure 5.7: The desorption sequence (a) Fiber core with weakly attached atoms and nanoclusters, (b) desorption beam is turned on, (c) weakly attached atoms desorb, (d) nanoclusters evaporate, (e) atoms form a uniform layer, (f) atoms re-arrange over a period of time into nanoclusters.

within the fiber walls. When a desorption beam is coupled into the fiber, the wings of the transverse light mode interact with the surface Rb atoms and with the diffused atoms in the fiber walls. The fast desorption mechanism could then be a result of these surface atoms which undergo a relatively weak desorption due to photo-induced charge transfer from silica to Rb as discussed in [62] (Fig. 5.7(c)). The slower desorption mechanism possibly occurs due to resonant heating of nanoclusters due to size-based surface plasmon resonances [59] leading to the evaporation of the nanoclusters and resulting in a stronger desorption (Fig. 5.7(d)). The glass matrix may also play a role in sustaining the strong, slow desorption mechanism by acting as a reservoir of diffused atoms and replen-

ishing atoms that may be lost over time from the surface. The possibility of two different sources of Rb atoms, requiring different desorption and recovery times is corroborated by the desorption recovery data as shown in Fig. 5.5 and Fig. 5.6. Immediately after desorption, the atoms form a uniform coating on the core surface which is non-resonant with the probe and the fiber transmission remains high (Fig. 5.7(e)). Over a period of 2 hours, the Rb population on the glass redistributes such that it agglomerates into nanoclusters that display enhanced scattering of coupled light over the entire band-gap and can sustain another round of plasmon-resonance based desorption (Fig. 5.7(f)).

5.5 Intensity dependence of desorption

In order to generate a controlled OD by modulating the desorption beam, we calibrate the absorption as a function of desorption beam power at the input. It is important to note that the OD varies over the duration of the desorption pulse, and we measure the OD generated by the fast mechanism when it stabilizes 50 μs after the desorption beam is switched on. In the case of the second, stronger mechanism, we measure the maximum OD produced by scanning across the entire D_1 Rb line during a few-s desorption pulse and extracting OD information by fitting with Voigt absorption profiles as described previously [61]. In Fig. 5.8, OD is defined as optical depth as experienced by a light field on resonance on ^{85}Rb ($F=2 \rightarrow F'=1,2$) D_1 transition.

Figure 5.8(a) shows that for short desorption pulses, the OD generated varies approximately linearly with incident power. OD measurement with short pulses at higher powers is not possible with this method because the vapor com-

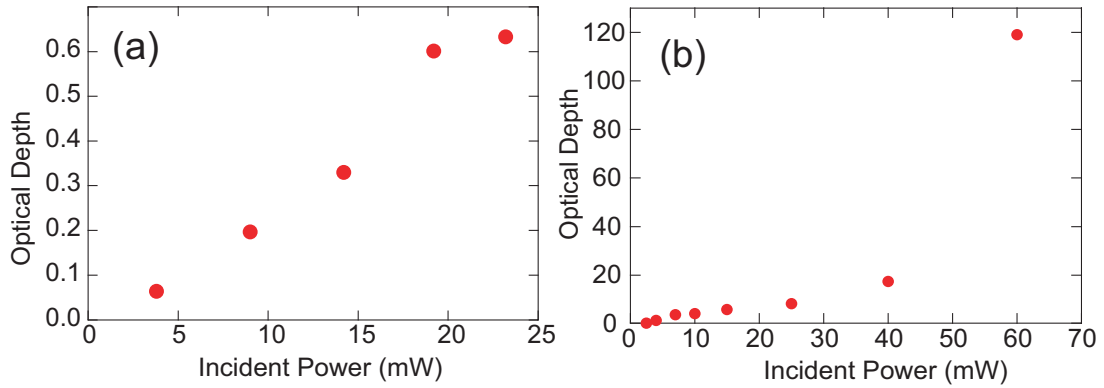


Figure 5.8: Optical depth generated as a function of incident desorption beam power in a coated fiber. (a) $50\text{-}\mu\text{s}$ pulses tuned on resonance are used to measure the absorption generated. The second, slower desorption mechanism does not contribute to this vapor generation. (b) Maximum steady OD generated by few-s long desorption pulses created by the second desorption mechanism.

pletely absorbs the probe, and the precise OD cannot be measured. Figure 5.8(b) shows the high ODs generated by the second mechanism, where the trend is linear until 40 mW, at which point the OD exhibits a large increase in sensitivity to the power. This may be due to bulk heating generated in the fiber, which can give rise to a thermally generated Rb vapor.

By tailoring the intensity and duration of the pulses, controllable optical depths can be generated in a repeatable fashion as shown in Fig. 5.9(a). Generating vapor via the fast mechanism using short desorption pulses ($< 50\ \mu\text{s}$) has the additional advantage that the fiber is not completely depleted and can desorb continuously for hours while still producing the same amount of vapor from shot to shot. On the other hand, the residual vapor that persists after a strong desorption pulse ($\sim 1\text{s}$) is switched off can be used for low-light-level nonlinear optical experiments while avoiding the scatter from the desorption beam. We perform electromagnetically induced transparency (EIT) in the Λ -

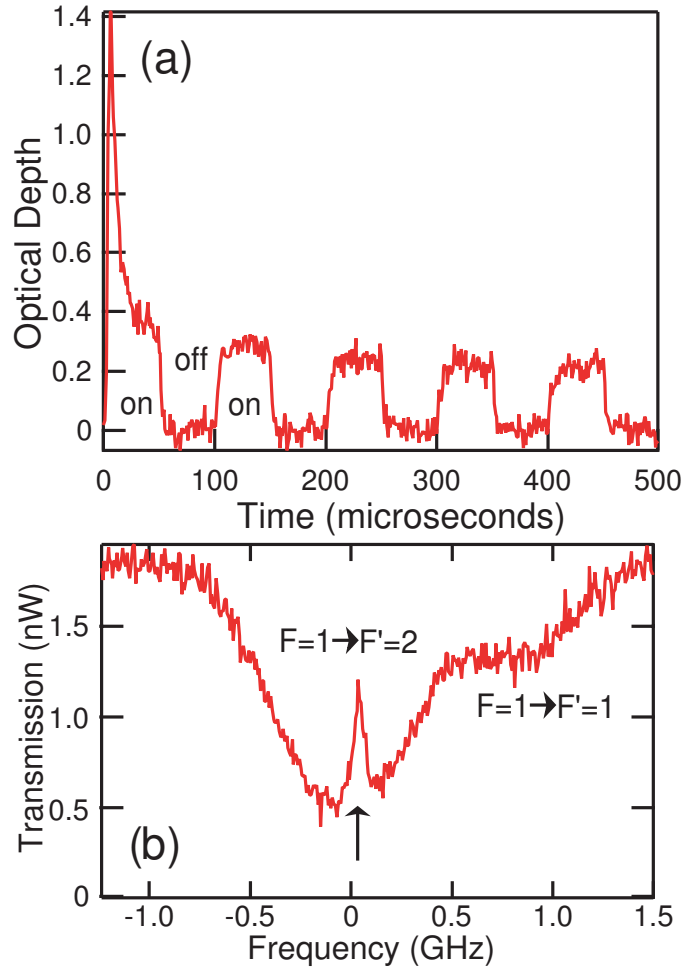


Figure 5.9: (a) Generation of controlled OD using 50- μ s, 10-mW desorption pulses in a coated fiber. We see that the OD generated is uniform during the pulse and from pulse-to-pulse. The large peak in OD at the beginning likely corresponds to Rb atoms that undergo fast desorption but do not regenerate within 500 μ s. (b) EIT in Λ -scheme (shown by the arrow) demonstrated in the residual vapor generated in a coated fiber after a strong desorption pulse. The oscilloscope is triggered after the desorption beam is completely switched off. A very low control beam power (80 nW, tuned to $F=2 \rightarrow F'=2$ transition) is used and the EIT peak shows no measurable light shift.

scheme in this residual vapor [see Fig. 5.9(b)]. The weak probe is scanned over the ($F=1 \rightarrow F'=1,2$) manifold of ^{87}Rb D_1 transition, while the control beam is

coupled co-propagating but cross-polarized to the probe beam and tuned to the ($F=2 \rightarrow F'=2$) transition of the D_1 line. Along with polarization isolation, we use an isotopically pure ^{85}Rb cell (broadened and shifted by 120 torr N_2) to selectively absorb the control beam and separate it from the probe [55]. We achieve a significant EIT depth (50 %) at 80 nW of pump power. The position of the EIT shows no light shifts as compared to when the desorption beam is on, thus demonstrating the advantage of using the residual vapor.

5.6 Summary

We have demonstrated on-demand and tunable Rb vapor generation that can be operated without depleting the fiber significantly. Additionally, we have shown that this vapor can be accessed in the absence of any desorption beam in the form of the residual vapor and have demonstrated Λ -scheme EIT in the residual vapor. We propose that two mechanisms exist for desorption in hollow-core bandgap fibers by analyzing the time-dynamics of desorption and the recovery data. The non-resonant atoms undergo a fast and weaker desorption, whereas the nanoclusters formed via redistribution of adsorbed atoms undergo a slower but stronger resonant desorption. We have also compared the effect of coating the fiber core on desorption and have not found significant difference in either the time-dynamics or band-gap measurements. The ability to conduct nanowatt-light-level nonlinear optical processes in fibers using a non-depleting high repetition rate desorption scheme is a significant advancement towards hollow-waveguide-based nonlinear optical systems.

CHAPTER 6

BUFFER-GAS EFFECTS OF NEON IN HC-PBGFS

Light-induced atomic desorption enables generation of very high densities of Rb vapor inside hollow-core photonic band-gap fibers. We have demonstrated that the atoms are generated with a velocity spread corresponding to an effective Maxwell-Boltzmann distribution temperature of ~ 500 K. Since the average velocity of atoms \bar{u} scales as $T^{1/2}$, the atoms spend less time in the beam at higher temperatures, which gives rise to transit-time broadening effects. Additionally, the rate of collisions with the walls is directly proportional to \bar{u} , which gives rise to collisional broadening effects due to electromagnetic interactions of the atoms with the walls. The self-assembled monolayers are ineffective in shielding the atoms from these effects possibly due to their small thickness even though hydrocarbons by themselves do not accept spin transfer from Rb atoms.

One of the earliest works on the reduction of transit-time across the beam was performed by W. Franzen [63], in which he studied the relaxation of optically pumped Rb atoms as a function of buffer gas pressures. The principle behind using a buffer gas is to provide impedance to the motion of Rb atoms across the beam due to collisions with the buffer gas atoms/molecules so that the atoms undergo slow diffusion. A comprehensive review on buffer gas effects has been published by Happer [39]. When using a buffer gas two competing phenomena need to be considered - diffusion due to buffer gases and decoherence due to collisions with buffer gas atoms. We would like to make the diffusion constant across the fiber to be as small as possible. For a given temperature, the diffusion constant D varies inversely as the pressure,

$$D = D_0 \frac{P_0}{P}, \quad (6.1)$$

where D_0 is the diffusion constant at atmospheric pressure P_0 . As the pressure increases, so does the probability of a ground-state spin-flip transition due to collisions with the buffer gas, which results in weaker EIT resonances [64, 65]. We want to find a regime where the optimal reduction in transit-time broadening can occur without significant contribution to the ground-state decoherence. Inert noble gases such as He, Ne, Ar are good candidates for buffer gases since they are diamagnetic [39] and cannot accept an angular momentum transfer from Rb atoms, hence avoiding a non-radiative transfer between the ground states. In fact, it takes about $10^7 - 10^8$ collisions with noble gas atoms before a spin-flip may occur [63, 64]. Using Ne as a buffer gas, the linewidth of coherent population trapping recently has been reduced to 50 Hz [66].

The treatment of depopulation of optically pumped vapor samples is performed using a diffusion equation [63]

$$\frac{\partial n_1}{\partial t} = D \nabla^2 n_1 - k n_1, \quad (6.2)$$

$$k = N_0 \sigma \bar{v}_{rel}(P/P_0), \quad (6.3)$$

where N_0 is the density of buffer-gas atoms at P_0 , σ is the disorientation cross-section on collisions with the buffer-gas atoms, and \bar{v}_{rel} is the relative velocity between Rb and buffer-gas atoms. Thus the second term is the decoherence term due to collisions with the buffer-gas atoms. The solutions of this equation in cylindrical geometry to the first order can be written in terms of the Bessel function $J_0(\mu r)$. The relaxation time τ can be written as

$$\tau = \frac{1}{(\mu_1^2 + \nu_1^2)D + k}, \quad (6.4)$$

where $\mu_1 a = 2.405$ (first zero of J_0), $a = 3 \mu\text{m}$ is the fiber radius, and $\nu_1 = \pi/L$, where $L = 25 \text{ cm}$. For an average velocity of $\bar{u} = 300 \text{ m/s}$, the time between collisions with the walls is $\sim 20 \text{ ns}$. The relaxation time must be significantly greater than this number in order to reduce the transit time broadening. Figure 6.1 shows the relaxation times τ that can be achieved using neon buffer gas as a function of pressure.

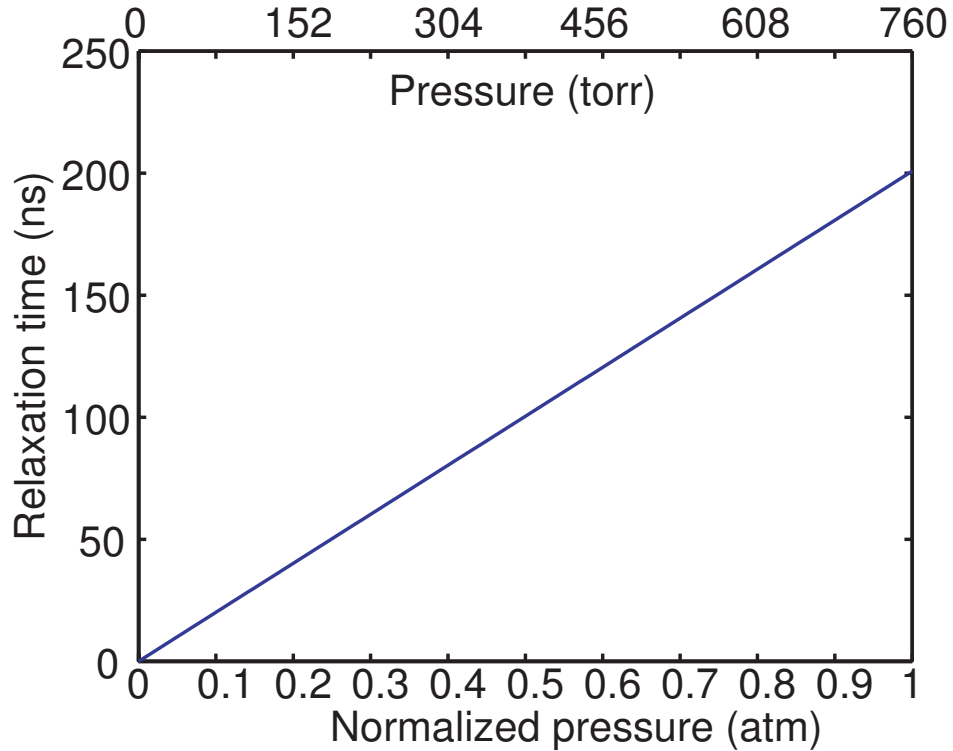


Figure 6.1: Relaxation times that can be achieved as a function of buffer gas pressure for a Rb vapor-Ne gas system. The neon vapor pressure is calculated at $50 \text{ }^\circ\text{C}$ which is the typical temperature at which the Rb cells are operated. The pressure is normalized to atmospheric pressure P_0 . For theory see Franzen [63].

We see that the relaxation time increases almost linearly with pressure till 1 atm (1.013×10^5 Pa). The relaxation time begins to saturate at 200 atm, beyond which collisional broadening starts contributing significantly to the decoherence process. One must keep in mind that as the diffusion process through the gas hinders the motion of atoms towards the fiber walls, it will also hinder the motion of atoms towards the beam center. Hence with increasing pressure, the desorbed atoms will find it difficult to enter the beam; and we must find a pressure regime where the atoms will be able to enter the beam but will be impeded in the process.

6.1 Experimental layout

For the buffer gas experiment, we revert back to the two cell design as discussed in chapter 3 with an additional connection for buffer gas to enter into the cell not connected to the Rb source. The individual cells can be separated from the vacuum system by valves (All-metal Swagelok), and each cell has a pressure gauge (Granville-Phillips, Swagelok-VCR vacuum connections) that can sense pressure from 0.1 torr to 1000 torr. The setup is shown in Fig. 6.2.

Initially, the right cell is sealed off from the vacuum system and the left cell is filled with buffer gas at an atmosphere and is flushed out through the vacuum system (with the turbomolecular pump off). This procedure is repeated 2-3 times to ensure that impurities such as any oxygen and water vapor that accumulate in the buffer-gas line due to possible leaks are flushed out before they contaminate the Rb in the right cell. Finally, both chambers are opened to the buffer-gas line while being shut off from the pumps, and the requisite

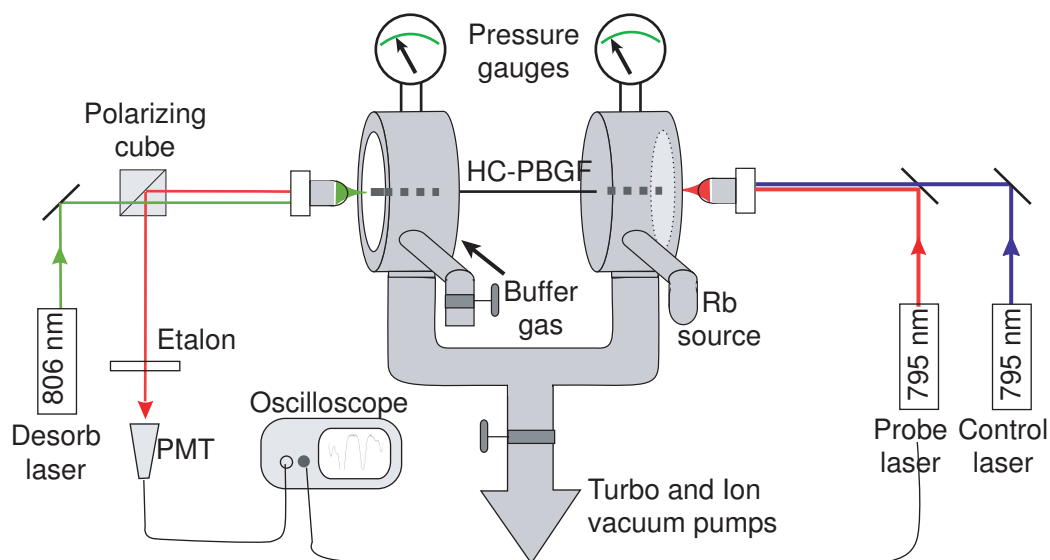


Figure 6.2: The two cells can be individually separated from the vacuum (valves not shown) so that the buffer-gas line can be flushed a number of times before the gas is introduced into the cell containing Rb vapor. Convectron pressure gauges on the cells monitor the pressure of buffer gas in the cells and are insensitive to Rb vapor. A Fabry-Perot etalon separates the probe and control beams before the PMT.

pressure of buffer-gas is introduced into the fiber from both ends. We found this method to work better than our initial attempts to introduce buffer gas into the Rb chamber directly, which caused the vapor to react with the contaminants and entirely disappear for a few hours. The signal and control beams are used in a Λ -configuration on the ^{87}Rb D_1 line which requires them to be separated using a temperature controlled etalon (BMV Optical, free spectral range = 40 GHz, bandwidth = 400 MHz).

6.2 Effect of buffer-gas on desorption

While performing desorption experiments in the presence of buffer gas, we found that the number of atoms desorbed (the highest flux as well as the cumulative total number) to be a strong function of the buffer-gas pressure introduced into the fibers. Initially, this was thought to be the same phenomenon as that observed when the buffer-gas line was not flushed, since the fiber Rb also reacted with the contaminants and was rendered unusable until more Rb was loaded from the front cells. However, careful experiments revealed that the phenomenon is reversible and the desorption capacity recovers as soon as the buffer-gas is evacuated from within the fiber.

Figure 6.3 shows the highest OD generated as a function of the buffer gas pressure present in the fiber. The desorption beam power was maintained constant throughout the experiment, and the OD and homogenous linewidths γ are obtained from theoretical fits to Voigt profiles. The OD shows a decreasing trend with increasing pressures, which is a behaviour in contrast to that observed by other researchers [45] who have observed that the atom number produced in bulk cells remains the same, but their transit time across the cell being slower means the absorption experienced by a probe is higher at higher pressures. At the same time, we observe that the homogenous linewidths show a strong upward trend as a function of buffer gas pressure, indicating that the excited state lifetimes undergo reduction with increasing pressure. Numerous effects could be responsible for this behavior of buffer-gas induced inhibition of LIAD. As discussed in the previous chapter, a possible mechanism for LIAD in hollow-core fibers could be resonant plasmon heating of nanoclusters which causes them to vaporize and generate a large Rb vapor density. At high pres-

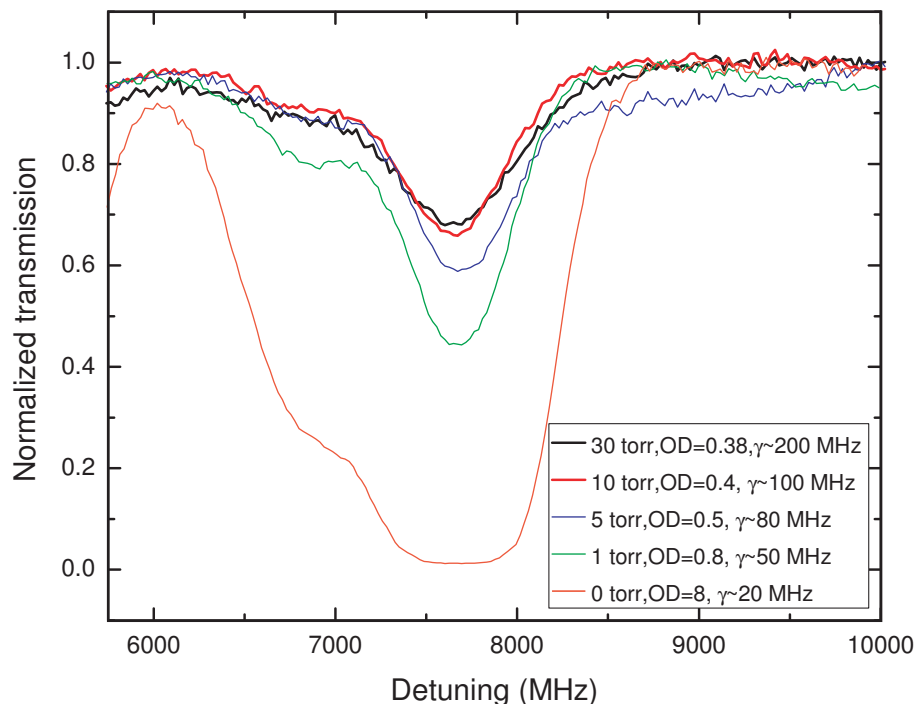


Figure 6.3: Generated optical depth as a function of buffer gas pressure. The desorption power was chosen such that the vapor produced for all pressures lies well within the dynamic range of the graph. The probe scans over the ^{87}Rb D_1 line ($F=1 \rightarrow F'=1,2$) transition. γ denotes the linewidth of the excited state due to buffer gas collisions, which is extracted from a theoretical fit to the absorption lines.

tures (> 50 torr), the heat mass presented by the buffer gas could act as a possible heat sink which can prevent the heating of nanoclusters and hence weaken the desorption effect. This could explain the pressure dependence since the higher the heat mass, the lower the temperature achieved by the nanoclusters and the lower would be the vapor density produced. Another mechanism that has been suggested for loss of vapor in the presence of a buffer-gas is dimer formation due to three-body collisions between two Rb atoms and a buffer-gas atom [67], which results in the removal of resonant atoms from the beam into non-resonant dimers. The pressure range of buffer gas for which such a behavior is expected

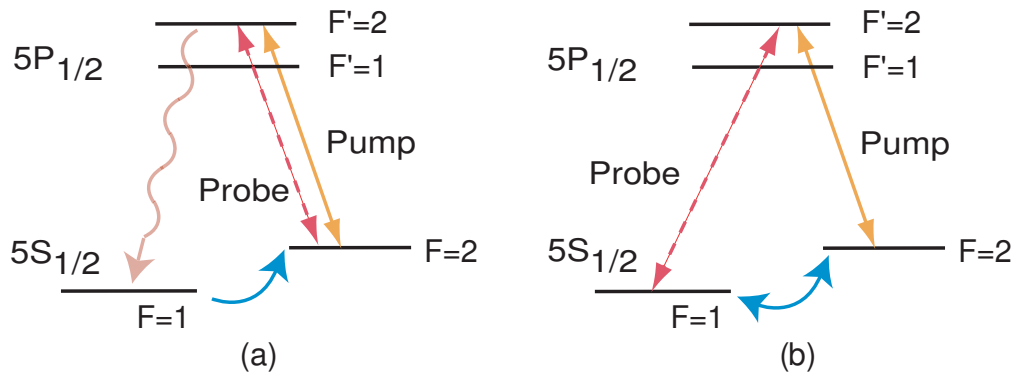


Figure 6.4: (a) A strong pumping beam pumps atoms into the $F=1$ ground state. Once the pump is turned off, a weak probe monitors the absorption as a function of time, which is a measure of rate of transfer of atoms from $F=1$ to $F=2$ ground state. (b) A Λ -scheme EIT sets up coherence between the two ground states wherein the ground-state decoherence and power broadening determine the EIT linewidth.

is found in our fibers ($> 10^{17}/\text{cc}$). The possibility of low vapor generation due to impurities as suggested by Sushkov and Budker [67] in buffer gases is unlikely, since the fiber undergoes strong desorption almost instantaneously after the buffer-gas is evacuated from the front cell with the mechanical pump. This would not be possible in the case of impurities because they would react with the adsorbed Rb atoms on the surface and make them unusable for desorption. The fiber would then have to be loaded from the ambient vapor before desorption can occur again.

6.3 Effect of buffer gas on the transit time of atoms

The effect of the buffer gas on the transit time of the atoms can be measured in two ways. One way is to optically pump the Rb atoms from one of the ground

states to the other ground state and observe the time signature of the relaxation of population back to the first ground state. As shown in Fig. 6.4 (a), a strong pump can optically pump atoms from $F = 2 \rightarrow F = 1$ state via an excited state. Once the process is complete, a weak probe can then measure the change in absorption on the $F = 2 \rightarrow F' = 2$ transition as the atoms undergo relaxation back to $F = 2$ state as shown by the blue arrow. The second method, which we use in this chapter, is shown in Fig. 6.4 (b) in which we directly measure the linewidth of the EIT as a function of buffer gas pressure. The dependence of EIT linewidth on various decoherence and power broadening mechanisms has been treated by Javan *et al.* [49]. Here, the authors have derived an analytical expression for the EIT linewidth under the assumption that the Doppler distribution can be approximated by a Lorentzian where the contribution from the wings is negligible (at low optical depths). The EIT linewidth Γ_{EIT} can be written as

$$\sqrt{\frac{2\gamma_{bc}}{\gamma}}\Omega \quad (\Omega^2\gamma/2\gamma_{bc}W_D^2 \ll 1), \quad (6.5)$$

$$\frac{\Omega^2}{W_D} \quad (\Omega^2\gamma/2\gamma_{bc}W_D^2 \gg 1), \quad (6.6)$$

where γ_{bc} is the ground-state decoherence rate, γ is the excited state decay rate, Ω is the control field Rabi frequency and W_D is the Doppler linewidth. Hence, a change in γ_{bc} can be monitored by measuring the EIT linewidth as a function of buffer gas pressure as long as the control beam power is low. The actual condition that needs to be satisfied is $\Omega^2\gamma/2\gamma_{bc}W_D^2 \ll 1$, which can be achieved in our case because γ_{bc} is larger than γ as shown in chapter 3.

The data are calibrated using a saturated absorption spectroscopy [47] setup as a frequency reference for the frequency-scanning axis (time axis). The probe

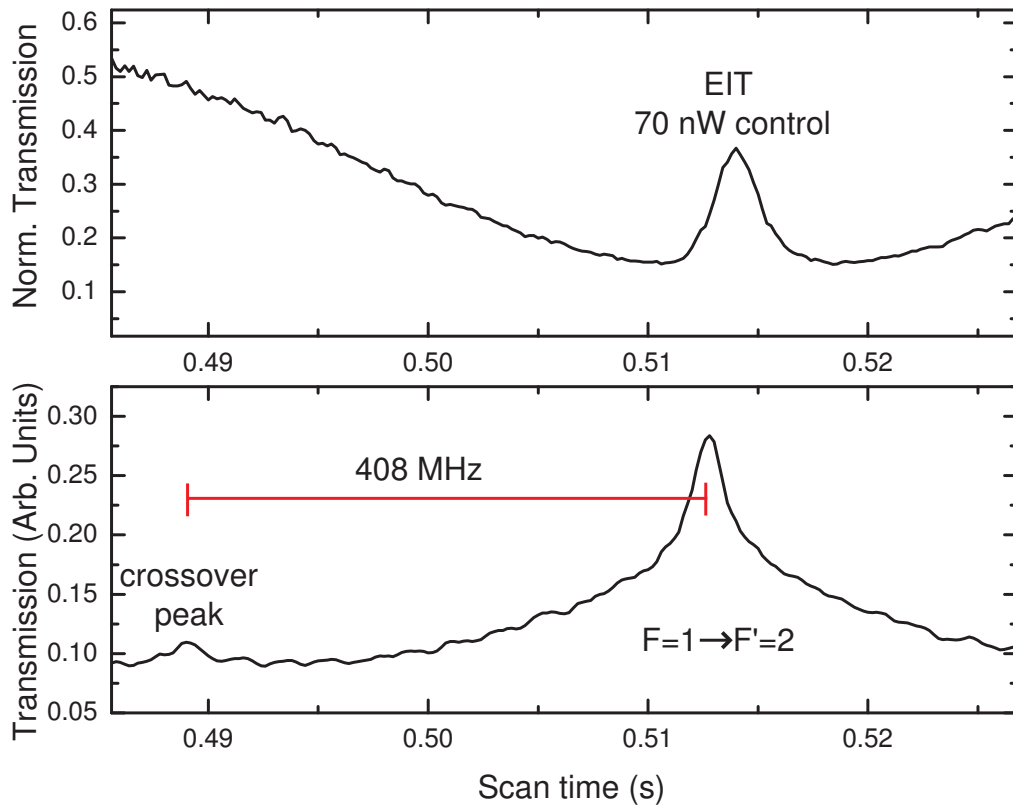


Figure 6.5: A 70-nW EIT feature on the $F = 1 \rightarrow F' = 1$ transition. The corresponding saturated absorption signal (SAS) obtained in a vapor cell is shown in the lower graph and used as the frequency reference. The EIT feature and the center of the Doppler line are offset from the SAS due to control field detuning and AC Stark shift from the desorption beam, respectively.

is scanned over the $F = 1 \rightarrow F' = 1, 2$ transition. Figure 6.5 shows the scan, and the corresponding saturated absorption scan used as a frequency reference. To extract the highest frequency resolution, the scan range is reduced as much as possible and is stopped at the cross-over resonance between $F' = 1$ and $F' = 2$ and reversed in direction. A 3-s long data acquisition (consisting of many 250-ms-long frequency scans) enables one to observe the Rb-vapor evolution over time and the EIT signal is normalized to a pure etalon scan to retrieve the

Doppler-broadened line with the EIT feature.

Figure 6.6 shows the data for EIT linewidth full width half maximum (FWHM) without buffer gas and 50 torr of buffer gas. The data are measured as a function of control beam power to measure power broadening effects. Since the EIT FWHM is proportional to Ω at low control beam powers, it should be proportional to $\sqrt{P_{control}}$. The solid line shows a fit to $A + B\sqrt{P_{control}}$ where the constant B is proportional to $\sqrt{\gamma_{bc}/\gamma}$ and A accounts for other sources of broadening such as laser linewidths. From the fits, we see that the $B = 2 \pm 0.5$ for 50 torr of Ne buffer gas, whereas $B = 5 \pm 1$ without the buffer gas. We observe that the presence of the buffer gas results in the narrowing of the EIT linewidth.

As shown in Fig. 6.3, the buffer gas strongly affects the excited state lifetime, and γ increases as the buffer gas pressure increases. Also, from Fig. 6.1, we expect the diffusion time at 50 torr of Ne gas pressure to be of the order of 10 ns. When added to the drift time of 20 ns across the fiber core, the increase in transit time by a factor of 1.5 does not account for the reduction in the EIT linewidth by a factor of 2.5 entirely. This implies that the remaining linewidth reduction must occur due to the significant increase in γ of the excited state. In fact, an increase in γ by a factor of 10 as shown in Fig. 6.3 could entirely account for a reduction in the EIT linewidth by a factor of 3. 50 torr is the upper limit to which one may pressurize the fiber and still achieve measureable optical depths due to LIAD. The reduction in linewidth can be useful for improving the performance of incoherent processes such as slow light, but processes that depend on improved ground-state coherence such as pulse storage and 4-level switching schemes do not benefit as much. Additionally, the loss in optical depth (by 3 orders of magnitude) due to the buffer gas cannot be compensated via the linewidth reduction

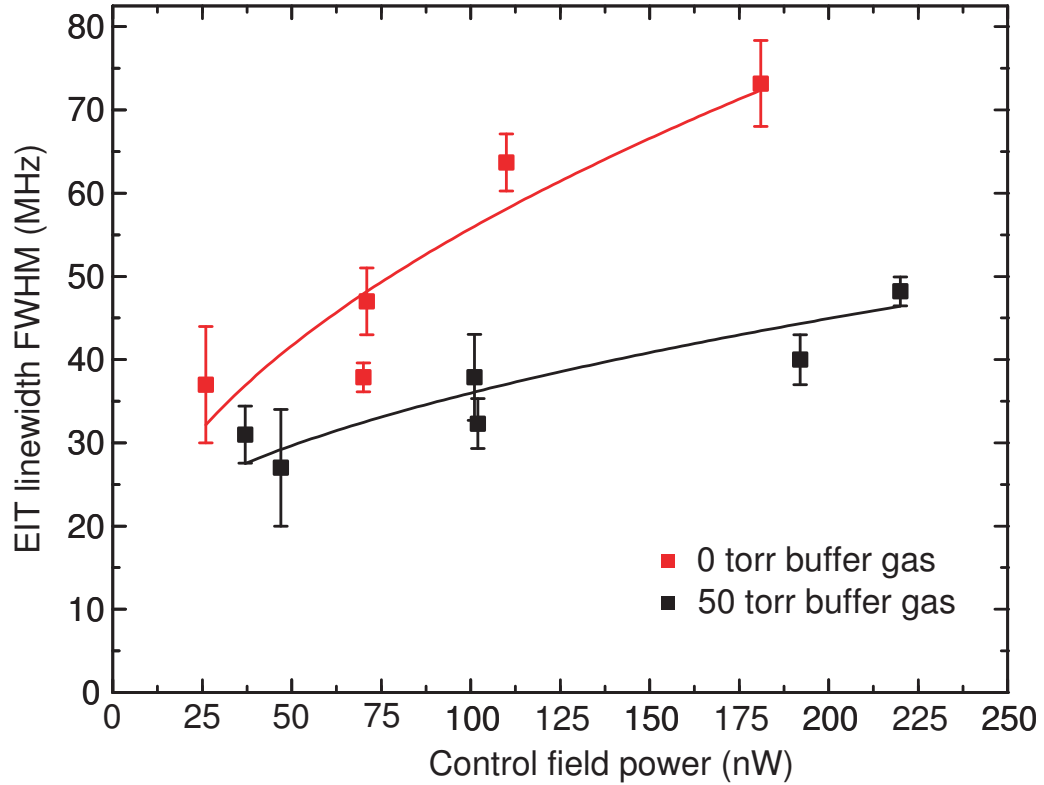


Figure 6.6: The EIT linewidth FWHM plotted as a function of control beam power. The data in red squares represent the linewidths in the absence of any buffer gas while those in black squares represent the linewidths at 50 torr of Ne buffer gas. The solid lines of the corresponding colors represent the fits to an expression of the form $A + B\sqrt{P_{control}}$ where B is proportional to $\sqrt{\gamma_{bc}/\gamma}$.

alone and as such, the buffer gas has an overall deleterious effect on nonlinear processes inside the fiber.

6.4 Summary

In this chapter, we investigated the effects of buffer gas on the ground-state coherence by measuring the EIT linewidths. We observe that the presence of the

buffer gas hinders the light-induced desorption of atoms from the fiber walls, which is a phenomenon that is not well understood. We also observe that the buffer gas results in reduction of the EIT linewidth via two processes - by increasing the transit time, but more importantly, via increase in the excited state decay rate. We conclude that the slight reduction in transit-time broadening is overwhelmingly negated by the significant reduction in the OD generated and as such the buffer gas has an overall negative effect on the atom-fiber system.

CHAPTER 7

FUTURE DIRECTIONS

In this thesis we have described a unique geometry for performing non-linear optical interactions at very low light powers using atomic vapors confined inside hollow-core photonic bandgap fibers. The vapor is produced using light-induced atomic desorption, and we have demonstrated optical depths in excess of 1000. We have also demonstrated nonlinear effects such as electromagnetically-induced transparency with control powers 1000 times lower than those used in glass vapor cells. Such a system presents definite advantages over vapor cells for agile and on-demand generation of optical depth on the order of milliseconds. Attempts to mitigate various decoherence mechanisms using organic coatings and buffer gases have proved ineffective, and the search for other techniques to achieve similar results continues.

Currently, our estimates show that only the first few mm of the fiber contribute towards the desorption process and a more direct measurement is necessary to map the contribution of the fiber along its length. An experiment for desorbing atoms from the side of the fiber has two important advantages: 1) the ability to monitor the longitudinal distribution of adsorbed Rb atoms; and 2) since desorption currently occurs due to the interaction of the wings of the Gaussian light mode with the adsorbed atoms, if the entire beam can illuminate the fiber walls, significantly lower optical powers will be required. Of course, the next logical step would be to investigate techniques for pushing the atoms further down the length of the fiber so that the entire length of the fiber can contribute to the optical depth. Possible techniques could include light-induced drift [42, 43] in the presence of buffer gases. If a significant portion of the fiber

length contributes to the desorption process, one could then accept the reduction in OD due to buffer gas and still generate enough OD at high buffer gas pressures to perform experiments with increased ground-state coherence. Also for trapping atoms in a dipole trap in the presence of a dissipative buffer gas, enough slow moving atoms could be released along the entire length of the fiber to produce a considerable OD of trapped cold atoms confined to the core.

Similarly, experiments with four-wave mixing (FWM) are currently being pursued in the hollow-core fiber system [68]. The FWM can take advantage of the bandwidth of the system to generate parametric amplification with over 300 MHz of bandwidth. Undoubtedly, this system can take advantage of improved optical pumping to make the process more efficient. But more importantly, such a system could be used to generate entangled photon pairs using spontaneous FWM [69] with ultra-low pump powers over a very large bandwidth, which is difficult to achieve in hot vapor cells [70].

Another direction that can be explored is the use of ring resonator cavities [71, 72] in conjunction with initially hot vapors and eventually cold atom clouds. Very high finesse Si:N ring resonators can be fabricated which can increase the atom-photon interaction greatly. One of the disadvantages of using tapered fibers [73, 74] or fabricated ring resonator structures is that hot atoms enter and leave the evanescent field zone very quickly and give rise to a very large transit-time decoherence. Assembling a cold-atom cloud near the ring resonator to reduce the decoherence could lead to a silicon-compatible on-chip device for performing low-light-level nonlinear interactions.

APPENDIX A

CHEMISTRY PROTOCOL FOR COATING THE FIBER CORES

Chemicals required:

1. 1M conc. HCl
2. n-Octadecyldimethylmethoxysilane (ODMS) (Supplier: Gelest Inc.)
3. Tetrahydrofuran (THF, used as the solvent)

Procedure:

1. 200 μL of ODMS is added to 5 mL HCl and the resulting solution is diluted to 25 mL with THF
2. Stir the solution thoroughly with a Teflon-coated magnetic stirrer for 5 minutes. This functionalizes the methyl group to react with silica ^-OH bonds
3. Dilute 2 mL of the above solution to 25 mL with THF and stir thoroughly.
4. The above solution is allowed to flow through the hollow-core fiber using a polyolefin syringe and microfluidic PEEK swaged fittings under pressure for 20 minutes and then allowed to incubate in the fiber for 20 minutes. This sequence is repeated so that fresh ODMS can reach the fiber sites each time pressure is applied.
5. The fiber is then flushed using pure THF from a separate syringe
6. The fiber is flushed with dry nitrogen for 1 day

BIBLIOGRAPHY

- [1] D. Bouwmeester, *The physics of quantum information* (Oxford, 1999).
- [2] H. Metcalf and E. Van der Stratten, *Laser cooling and trapping* (Oxford, 1999).
- [3] P. Russell, *Science* **299**, 358 (2003).
- [4] P. Russell, *J. Lightw. Tech* **24**, 4729 (2006).
- [5] N. W. Ashcroft and N. D. Mermin, *Solid State Physics* (Brooks Cole, 1976).
- [6] P. W. Anderson, *Phys. Rev.* **109**, 1492 (1958).
- [7] N. F. Mott, *Adv. Phys.* **16**, 49 (1967).
- [8] P. Yeh and A. Yariv, *Opt. Commun.* **19**, 427 (1976).
- [9] E. Yablonovitch, *Phys. Rev. Lett.* **58**, 2059 (1987).
- [10] S. John, *Phys. Rev. Lett.* **58**, 2486 (1987).
- [11] R. F. Cregan, B. J. Mangan, J. C. Knight, T. A. Birks, P. S. J. Russell, P. J. Roberts, and D. C. Allan, *Science* **285**, 1537 (1999).
- [12] C. J. Hensley, D. G. Ouzounov, A. L. Gaeta, N. Venkataraman, M. T. Gallagher, and K. W. Koch, *Opt. Express* **15**, 3507 (2007).
- [13] A. R. Bhagwat and A. L. Gaeta, *Opt. Express* **16**, 5035 (2008).
- [14] J. D. Jackson, *Classical Electrodynamics* (John Wiley and Sons, Inc, 1998).
- [15] R. W. Boyd, *Nonlinear Optics* (Academic Press, 2003).
- [16] J. J. Sakurai, *Modern Quantum Mechanics* (Addison-Wesley Publishing Company, 1985).

- [17] U. Fano, Phys. Rev. **124**, 1866 (1961).
- [18] A. Imamoğlu and S. E. Harris, Opt. Lett. **14**, 1344 (1989).
- [19] K.-J. Boller, A. Imamoğlu, and S. E. Harris, Phys. Rev. Lett. **66**, 2593 (1991).
- [20] M. Fleischhauer, A. Imamoğlu, and J. P. Marangos, Rev. Mod. Phys. **77**, 633 (2005).
- [21] S. E. Harris, J. E. Field, and A. Imamoğlu, Phys. Rev. Lett. **64**, 1107 (1990).
- [22] L. V. Hau, S. E. Harris, Z. Dutton, and C. H. Behroozi, Nature **397**, 594 (1999).
- [23] M. Fleischhauer and M. D. Lukin, Phys. Rev. Lett. **84**, 5094 (2000).
- [24] C. Liu, Z. Dutton, C. H. Behroozi, and L. V. Hau, Nature **409**, 490 (2001).
- [25] J. McKeever, A. Boca, A. D. Boozer, R. Miller, J. R. Buck, A. Kuzmich, and H. J. Kimble, Science **303**, 1992 (2004).
- [26] S. E. Harris and Y. Yamamoto, Phys. Rev. Lett. **81**, 3611 (1998).
- [27] H. Schmidt and A. Imamoğlu, Opt. Lett. **21**, 1936 (1996).
- [28] F. Benabid, J. C. Knight, G. Antonopoulos, and P. S. J. Russell, Science **298**, 399 (2002).
- [29] F. Benabid, G. Bouwmans, J. C. Knight, P. S. J. Russell, and F. Couny, Phys. Rev. Lett. **93**, 123903 (2004).
- [30] S. Ghosh, J. E. Sharping, D. G. Ouzounov, and A. L. Gaeta, Phys. Rev. Lett. **94**, 093902 (2005).
- [31] F. Benabid, P. Light, F. Couny, and P. Russell, Opt. Express **13**, 5694 (2005).

- [32] D. G. Ouzounov, F. R. Ahmad, D. Muller, N. Venkataraman, M. T. Gallagher, M. G. Thomas, J. Silcox, K. W. Koch, and A. L. Gaeta, *Science* **301**, 1702 (2003).
- [33] F. Benabid, J. Knight, and P. Russell, *Opt. Express* **10**, 1195 (2002).
- [34] S. Mandal and D. Erickson, *Appl. Phys. Lett.* **90**, 184103 (2007).
- [35] G. Herzberg, *Atomic Spectra and Atomic Structure* (Dover Publications, 1944).
- [36] D. A. Steck, *Rubidium D line data*, URL <http://steck.us/alkalidata/>.
- [37] E. B. Alexandrov, M. V. Balabas, D. Budker, D. English, D. F. Kimball, C.-H. Li, and V. V. Yashchuk, *Phys. Rev. A* **66**, 042903 (2002).
- [38] M. J. Renn, D. Montgomery, O. Vdovin, D. Z. Anderson, C. E. Wieman, and E. A. Cornell, *Phys. Rev. Lett.* **75**, 3253 (1995).
- [39] W. Happer, *Rev. Mod. Phys.* **44**, 169 (1972).
- [40] M. A. Bouchiat and J. Brossel, *Phys. Rev.* **147**, 41 (1966).
- [41] J. C. Camparo, *J. Chem. Phys.* **86**, 1533 (1987).
- [42] F. K. Gel'mukhanov and A. M. Shalagin, *JETP Lett.* **29**, 711 (1979).
- [43] H. G. C. Werij, J. E. M. Haverkort, and J. P. Woerdman, *Phys. Rev. A* **33**, 3270 (1986).
- [44] A. Gozzini, F. Mango, J. H. Xu, G. Alzetta, F. Maccarrone, and R. A. Bernheim, *Il Nuovo Cimento D* **15**, 709 (1993).

- [45] S. N. Atutov, V. Biancalana, P. Bicchi, C. Marinelli, E. Mariotti, M. Meucci, A. Nagel, K. A. Nasyrov, S. Rachini, and L. Moi, *Phys. Rev. A* **60**, 4693 (1999).
- [46] C. R. Kessel and S. Granick, *Langmuir* **7**, 532 (1991).
- [47] W. Demtröder, *Laser Spectroscopy* (Springer-Verlag, 1996).
- [48] D. J. Fulton, S. Shepherd, R. R. Moseley, B. D. Sinclair, and M. H. Dunn, *Phys. Rev. A* **52**, 2302 (1995).
- [49] A. Javan, O. Kocharovskaya, H. Lee, and M. O. Scully, *Phys. Rev. A* **66**, 013805 (2002).
- [50] A. Burchianti, C. Marinelli, A. Bogi, J. Brewer, K. Rubahn, H.-G. Rubahn, F. della Valle, E. Mariotti, V. Biancalana, S. Veronesi, et al., *Europhys. Lett.* **67**, 983 (2004).
- [51] A. Hatakeyama, M. Wilde, and K. Fukutani, *e-J. Surf. Sci. Nanotech.* **4**, 63 (2006).
- [52] D. A. Steck, *Rubidium 87 D line data*, URL <http://steck.us/alkalidata/rubidium87numbers.pdf>.
- [53] M. Faheem, R. Thapa, and K. L. Corwin, in *Conference on Lasers and Electro-Optics/Quantum Electronics and Laser Science and Photonic Applications Systems Technologies* (Optical Society of America, 2005), p. CWJ6.
- [54] V. S. Letokhov, *High-Resolution Laser Spectroscopy* (Springer-Verlag, New York, 1976).
- [55] N. Kuramochi, S. Naritsuka, and N. Oura, *Opt. Lett.* **6**, 73 (1981).

- [56] A. B. Matsko, I. Novikova, M. O. Scully, and G. R. Welch, *Phys. Rev. Lett.* **87**, 133601 (2001).
- [57] S. Ghosh, A. R. Bhagwat, C. K. Renshaw, S. Goh, A. L. Gaeta, and B. J. Kirby, *Phys. Rev. Lett.* **97**, 023603 (2006).
- [58] *Air-6-800 fiber datasheet*, URL <http://www.crystal-fibre.com/datasheets/AIR-6-800.pdf>.
- [59] A. Burchianti, A. Bogi, C. Marinelli, C. Maibohm, E. Mariotti, and L. Moi, *Phys. Rev. Lett.* **97**, 157404 (2006).
- [60] A. Burchianti, A. Bogi, C. Marinelli, C. Maibohm, E. Mariotti, S. Sanguinetti, and L. Moi, *Eur. Phys. J. D* **49**, 201 (2008).
- [61] A. D. Slepko, A. R. Bhagwat, V. Venkataraman, P. Londero, and A. L. Gaeta, *Opt. Express* **16**, 18976 (2008).
- [62] B. V. Yakshinskiy and T. E. Madey, *Nature* **400**, 642 (1999).
- [63] W. Franzen, *Phys. Rev.* **115**, 850 (1959).
- [64] J. H. Xu and G. Alzetta, *Phys. Lett. A* **248**, 80 (1998).
- [65] G. G. Padmabandu, X. Li, C. Su, E. S. Fry, D. E. Nikonov, S.-Y. Zhu, G. M. Meyer, and M. O. Scully, *Quantum Opt.* **6**, 261 (1994).
- [66] S. Brandt, A. Nagel, R. Wynands, and D. Meschede, *Phys. Rev. A* **56**, R1063 (1997).
- [67] A. O. Sushkov and D. Budker, *Phys. Rev. A* **77**, 042707 (2008).
- [68] P. Londero, V. Venkataraman, A. R. Bhagwat, A. D. Slepko, and A. L. Gaeta, *Phys. Rev. Lett.* **103**, 043602 (2009).

- [69] J. Fan and A. Migdall, *Opt. Express* **15**, 2915 (2007).
- [70] C. F. McCormick, V. Boyer, E. Arimondo, and P. D. Lett, *Opt. Lett.* **32**, 178 (2007).
- [71] V. R. Almeida, C. A. Barrios, R. R. Panepucci, and M. Lipson, *Nature* **431**, 1081 (2004).
- [72] A. Gondarenko, J. S. Levy, and M. Lipson, *Opt. Express* **17**, 11366 (2009).
- [73] S. M. Spillane, G. S. Pati, K. Salit, M. Hall, P. Kumar, R. G. Beausoleil, and M. S. Shahriar, *Phys. Rev. Lett.* **100**, 233602 (2008).
- [74] S. M. Hendrickson, T. B. Pittman, and J. D. Franson, *J. Opt. Soc. Am. B* **26**, 267 (2009).